Research Square

Preprints are preliminary reports that have not undergone peer review.
They should not be considered conclusive, used to inform clinical practice,
or referenced by the media as validated information.

Equilibrium Bifurcations and Periodic Dynamics in a Planar Restricted Five-Body Problem with Four Unequal Primaries

Muhammad Shoaib
A. R. Kashif
kashmology@gmail.com

Capital University of Science and Technology

Research Article

Keywords:

Posted Date: November 6th, 2026

DOI: https://doi.org/10.21203/rs.3.rs-11621928/v1

License: This work is licensed under a Creative Commons Attribution 4.0 International License.
Read Full License

Additional Declarations: No competing interests reported.

Equilibrium Bifurcations and Periodic Dynamics in a Planar Restricted Five-Body Problem with Four Unequal Primaries

Muhammad Shoaib*
Smart and Scientific Solutions, 14 Quarry Place, Hamilton ML3 7BB, UK

A. R. Kashif
Department of Mathematics, Capital University of Science and Technology,
Zone-V, Islamabad, Pakistan

November 4, 2026

Abstract

We derive a general model for the planar restricted five-body problem with four unequal primaries in a non-symmetric coplanar central configuration. Four primaries form an admissible central configuration, and a fifth infinitesimal body moves in their gravitational field. We translate the primary configuration to its centre of mass and normalise the masses so that the primaries remain fixed in a frame rotating with unit angular velocity. We derive analytical conditions for the number and type of equilibrium points and for their spectral stability. We show that the number of nondegenerate equilibria is odd, that every generic fold creates or destroys one minimum and one saddle, and that spectral stability is possible only at a minimum. Numerical continuation on two separate positive-mass arcs gives as many as fifteen equilibrium points. Spectral stability occurs on a single equilibrium branch and is lost through a Hamiltonian–Hopf collision. We compute local Lyapunov families arising from the centre modes and classify them using their Floquet multipliers and Hill regions. We also obtain large-scale rosette-type circulating periodic families independently from resonant Kepler seeds.

Keywords: restricted five-body problem; central configuration; equilibrium bifurcation; spectral stability; periodic orbit; Hill region.

Mathematics Subject Classification (2020): 70F10; 70F15; 70K42; 37N05; 65P30.

1 Introduction

The restricted n-body problem describes the motion of an infinitesimal body in the gravitational field of massive primaries moving in a prescribed relative equilibrium. Such models have long been used to study the structure of celestial-mechanical phase space. In the circular restricted three-body problem, the five Lagrange equilibrium points, their linear stability, the associated zero-velocity curves and Hill regions, and the periodic orbits arising from the centre modes are all well understood [17, 9]. Higher restricted problems lead to the same questions, but the answers also depend on the geometry and mass distribution of the primaries. The number and type of equilibrium points, their stability, and the nearby periodic motion may therefore change as the primary configuration is varied.

*Current address: Centre of Data Science, Government College University Faisalabad (GCUF), Faisalabad, Pakistan.

This dependence is already apparent in the restricted four-body problem. For three primaries at the vertices of an equilateral triangle, Baltagiannis and Papadakis [2, 3] determined how the location, number and stability of the equilibrium points vary with the primary mass ratios, and computed families of periodic orbits for unequal masses. The restricted five-body problem introduces a further degree of geometric freedom. Ollongren [12] showed that a symmetric arrangement of four primaries can support nine equilibrium points, some of which are stable. Kalvouridis [6] studied the regular-polygon ring problem, while Zotos and Suraj [19] and Zotos and Papadakis [18] examined basins of attraction and periodic-orbit networks for symmetric arrangements. Kashif and Shoaib [7] considered a concave kite arrangement of four primaries. In all these restricted five-body models, the primary geometry is prescribed and possesses a symmetry.

Four primaries cannot, however, be placed arbitrarily if they are to remain fixed in a uniformly rotating frame. Their positions and masses must form a central configuration. Four-body central configurations have consequently been studied from the collinear solutions of Moulton [11] to the relative equilibria of Simó [15], the degeneracy results of Palmore [13], and the finiteness theorem of Hampton and Moeckel [5]. Symmetric families have also been examined by Steves and Roy [16] and Benhammouda et al. [4]. A symmetry assumption makes the central-configuration problem easier to treat, but it excludes many possible geometries and mass distributions.

The general coplanar construction of Shoaib et al. [14] removes this restriction. In that model, three primaries define a reference triangle and the fourth is allowed to occupy a general point in the plane. A scalar constraint, explicit mass-ratio formulae and positivity conditions then determine the admissible central configurations. Both convex and concave configurations are obtained, and the known symmetric configurations appear as special cases. This construction provides a natural basis for studying a restricted five-body problem without imposing symmetry on the primaries.

We determine how the equilibrium structure and periodic dynamics of the infinitesimal body change as a general non-symmetric central configuration is continuously deformed. A comparison of isolated configurations is not sufficient for this purpose. Two configurations with different numbers of equilibrium points may lie on different connected components of the admissible set, while a single component may pass through several equilibrium multiplicities. We therefore trace the admissible primary configurations and the corresponding restricted equilibria together, using pseudo-arclength continuation supported by independent global equilibrium searches.

Some properties of the problem can be established analytically. The effective potential is strictly subharmonic and has no local maxima. Morse theory then shows that a nondegenerate configuration has an odd number of equilibrium points, with the saddles outnumbering the minima by three, and that a generic fold creates or destroys one minimum and one saddle. Spectral stability is possible only at a minimum and is determined by two inequalities involving the trace and determinant of the Hessian. These inequalities play the role of the classical Routh condition in the restricted three-body problem.

The remaining results are obtained numerically on a fixed slice of the central-configuration parameter space. The positive-mass configurations form two separate arcs. Along these arcs the number of equilibrium points changes only through nondegenerate saddle-node folds and reaches fifteen. Spectral stability occurs on one equilibrium branch and is lost through a Hamiltonian–Hopf collision of imaginary eigenvalues. Local Lyapunov families arising from the centre modes are then continued and classified by their Floquet multipliers and by the Hill regions accessible to them. At the same generic branch-24 configuration, additional large-scale rosette-type circulating families are obtained independently from resonant Kepler seeds.

The paper is organised as follows. Section 2 derives the barycentric unit-angular-rate formulation and establishes the analytical results used throughout the paper. Section 3 traces the admissible primary configurations, determines the equilibrium multiplicities, and locates the saddle-node folds.

Section 4 examines the linear spectrum and the loss of stability. Section 5 continues the local Lyapunov families, studies their Floquet multipliers, and constructs the rosette-type circulating families. Section 6 describes the critical Jacobi levels and the corresponding Hill-region topology. The conclusions are given in Section 7.

2 Mathematical model

We consider an infinitesimal fifth body moving in the planar gravitational field of four massive primaries. The primaries form a non-collinear four-body central configuration (CC) and hence generate a rigidly rotating relative equilibrium about their common centre of mass. The geometric CC construction reviewed in Section 2.1 is due to Shoaib et al. [14]; it is restated only to define the admissible primary family and fix notation. Section 2.2 derives the additional barycentric and mass-scale normalisation required before that construction can be used as a unit-angular-rate restricted problem.

2.1 The primary central configuration

Using the translation, rotation, reflection and scaling invariances of the planar CC equations, place the four primaries at

$$\mathbf{r}_0 = (0, b), \qquad \mathbf{r}_1 = (-1, 0), \qquad \mathbf{r}_2 = (0, a), \qquad \mathbf{r}_3 = (c_1, c_2), \tag{1}$$

where

$$a > 0, \qquad b < a, \qquad b \neq \pm a.$$

The condition $\mathbf{r}_1 = (-1, 0)$ fixes the geometric length scale, $\mathbf{r}_0$ and $\mathbf{r}_2$ lie on the y-axis, and $\mathbf{r}_3$ remains free in the plane. The primary geometry is therefore described by

$$p = (a, b, c_1, c_2).$$

Figure 1 compares these position coordinates with the barycentric frame used for the restricted dynamics.

For compactness, define the following cubes of mutual distances:

$$\begin{aligned} \sigma &= (1 + a^2)^{3/2}, & \varsigma &= (1 + b^2)^{3/2}, & \tau &= (a - b)^3, \\ G_c &= \left[c_1^2 + (c_2 - a)^2\right]^{3/2}, & T_c &= \left[c_1^2 + (c_2 - b)^2\right]^{3/2}, & M_c &= \left[(c_1 + 1)^2 + c_2^2\right]^{3/2}. \end{aligned} \tag{2}$$

The subscripts distinguish these geometric quantities from the gravitational constant and total mass introduced below.

To make the construction self-contained, let $d_{ij} = |\mathbf{r}_i - \mathbf{r}_j|$ and let $\Lambda_{ijk} = (\mathbf{r}_i - \mathbf{r}_j) \wedge (\mathbf{r}_i - \mathbf{r}_k)$ denote the signed double area of the triangle formed by primaries i, j, k; the symbol is chosen to avoid the admissible set $\mathcal{A}$ defined below. In an arbitrary coordinate system the central-configuration equations are

$$\sum_{j \neq i} m_j \frac{\mathbf{r}_j - \mathbf{r}_i}{d_{ij}^3} = -\kappa(\mathbf{r}_i - \mathbf{c}), \qquad i = 0, \ldots, 3, \tag{3}$$

where $\mathbf{c}$ is the primary barycentre and $\kappa > 0$ is the common multiplier. Subtracting the equations for primaries i and j, and taking the planar wedge product with $\mathbf{r}_i - \mathbf{r}_j$, eliminates both $\mathbf{c}$ and κ. This gives the Laura–Andoyer relations

$$\sum_{k \neq i,j} m_k \left(\frac{1}{d_{ik}^3} - \frac{1}{d_{jk}^3} \right) \Lambda_{ijk} = 0, \qquad 0 \leq i < j \leq 3. \tag{4}$$

The Dziobek reduction consists of inserting the position coordinates (1) into these relations and eliminating the masses. Since (4) is homogeneous in the masses, only the ratios

$$\rho_0 = \frac{m_0}{m_3}, \qquad \rho_1 = \frac{m_1}{m_3}, \qquad \rho_2 = \frac{m_2}{m_3} \tag{5}$$

are determined. Three independent relations are linear in ρ_0, ρ_1, ρ_2 and determine them. Substitution into a remaining independent relation supplies the compatibility condition for the geometry. For the nondegenerate geometries considered here, simplifying that condition gives

$$\begin{aligned}\psi(a,b,c_1,c_2) = {} & \tau(\sigma-\varsigma)M_c + T_c\big[(\tau-\sigma)M_c + \sigma(\varsigma-\tau)\big] \\ & + G_c\big[(\sigma-\varsigma)T_c + (\varsigma-\tau)M_c + \varsigma(\tau-\sigma)\big] = 0,\end{aligned} \tag{6}$$

with the corresponding ratios

$$\begin{aligned}\rho_0 &= \frac{(c_2 - a - ac_1)(M_c - G_c)\varsigma\tau}{(a-b)(\varsigma-\tau)M_cG_c}, \\ \rho_1 &= \frac{c_1(G_c - T_c)\sigma\varsigma}{(\sigma-\varsigma)G_cT_c}, \\ \rho_2 &= \frac{(c_2 - b - bc_1)(M_c - T_c)\sigma\tau}{(a-b)(\tau-\sigma)M_cT_c}.\end{aligned} \tag{7}$$

Solving the three linear relations gives (7); their compatibility is precisely (6). Thus, subject to the stated nondegeneracy conditions, these formulae are equivalent to the planar CC equations and introduce no additional assumption. They agree with the closed form obtained by Shoaib et al. [14].

Not every point satisfying $\psi = 0$ yields a positive-mass, nondegenerate configuration. We define the admissible set by

$$\mathcal{A} = \{p : \ \psi(p) = 0, \quad \rho_0(p) > 0, \quad \rho_1(p) > 0, \quad \rho_2(p) > 0\}, \tag{8}$$

with the additional requirements that all denominators in (7) be nonzero and that no two primaries collide. Because the CC equations determine only ratios, we introduce the convenient representative

$$\widehat{\mathbf{m}} = (\widehat{m}_0, \widehat{m}_1, \widehat{m}_2, \widehat{m}_3) = (\rho_0, \rho_1, \rho_2, 1). \tag{9}$$

Thus $\widehat{m}_3 = 1$ selects one member of an arbitrary common-mass-scale class. It does not fix the angular velocity of the primary relative equilibrium and is not the final mass normalisation used in the restricted equations.

2.2 From mass ratios to a unit-rate relative equilibrium

The position coordinates (1) fix the geometry but are not generally barycentric. Let

$$\widehat{m}_{\mathrm{tot}} = \sum_{i=0}^{3} \widehat{m}_i, \qquad \mathbf{c} = \frac{1}{\widehat{m}_{\mathrm{tot}}} \sum_{i=0}^{3} \widehat{m}_i \mathbf{r}_i \tag{10}$$

and define the barycentric primary coordinates

$$\mathbf{q}_i = \mathbf{r}_i - \mathbf{c}, \qquad \sum_{i=0}^{3} \widehat{m}_i \mathbf{q}_i = \mathbf{0}. \tag{11}$$

Translation leaves all mutual primary separations unchanged, but it places the origin of the rotating frame at the point about which the primaries execute their relative equilibrium.

In the barycentric coordinates (11), and with the representative masses, the central-configuration equations (3) read

$$\mathbf{g}_i = -\kappa \mathbf{q}_i, \qquad \mathbf{g}_i = \sum_{j \neq i} \widehat{m}_j \frac{\mathbf{q}_j - \mathbf{q}_i}{|\mathbf{q}_j - \mathbf{q}_i|^3}, \qquad i = 0, \ldots, 3, \tag{12}$$

where $\mathbf{g}_i$ is the gravitational acceleration of primary i in units with $G = 1$. The reduction of Section 2.1 eliminated κ; to recover it, define

$$U = \sum_{0 \leq i < j \leq 3} \frac{\widehat{m}_i \widehat{m}_j}{|\mathbf{q}_i - \mathbf{q}_j|}, \qquad I = \sum_{i=0}^{3} \widehat{m}_i |\mathbf{q}_i|^2. \tag{13}$$

Multiplying (12) by $\widehat{m}_i \mathbf{q}_i$, summing over i, and pairing the two contributions from each unordered primary pair gives $-U = -\kappa I$, so

$$\kappa = \frac{U}{I}. \tag{14}$$

The conversion to a unit-rate problem is independent of the arbitrary scale chosen for the representative masses. Under $\widehat{\mathbf{m}} \mapsto s\widehat{\mathbf{m}}$, $s > 0$, the factors of s cancel in (10), while the accelerations and κ both acquire the factor s. Consequently,

$$\frac{s\widehat{m}_i}{s\kappa} = \frac{\widehat{m}_i}{\kappa}, \qquad i = 0, \ldots, 3. \tag{15}$$

Hence the ratios in (15) depend only on the mass-ratio class.

Let the unit distance in (1) represent a physical length L, and let the physical primary masses be $M_0 \widehat{m}_i$, where M_0 is an arbitrary common mass scale. If G is the gravitational constant and n is the angular speed of the primary relative equilibrium, dimensional centripetal balance gives

$$n^2 = \frac{GM_0}{L^3} \kappa. \tag{16}$$

After positions are divided by L and time is rescaled by $\tau = nt$, the dimensionless gravitational coefficient of primary i is therefore

$$\frac{GM_0 \widehat{m}_i}{n^2 L^3} = \frac{\widehat{m}_i}{\kappa} =: m_i^\star, \qquad i = 0, \ldots, 3. \tag{17}$$

Thus $m_i^\star$ are dimensionless unit-rate mass parameters, not the unscaled physical masses. In particular, $m_3^\star = 1/\kappa$, not unity. Dividing the central-configuration equations by κ gives

$$\sum_{j \neq i} m_j^\star \frac{\mathbf{q}_j - \mathbf{q}_i}{|\mathbf{q}_j - \mathbf{q}_i|^3} = -\mathbf{q}_i, \qquad i = 0, \ldots, 3, \tag{18}$$

so the same dimensionless primary geometry is stationary in the frame with unit angular rate. We use this form throughout because it preserves the standard Coriolis coefficients and is independent of the arbitrary choices of M_0 and representative mass scale.

2.3 Restricted fifth-body equations and equilibria

Figure 1 separates the two coordinate descriptions. The left panel shows the position coordinates $\mathbf{r}_i$ used to parameterise the central configuration, while the right panel shows the barycentric coordinates $\mathbf{q}_i = \mathbf{r}_i - \mathbf{c}$ used in the restricted equations. The figure is drawn to scale for the Case-2 reference configuration of Table 1, for which $\mathbf{c} = (-0.06, -0.02)$. Translation does not change the primary separations or the distances R_i, but it moves the origin of the centrifugal term from the geometric origin O to the barycentre C.

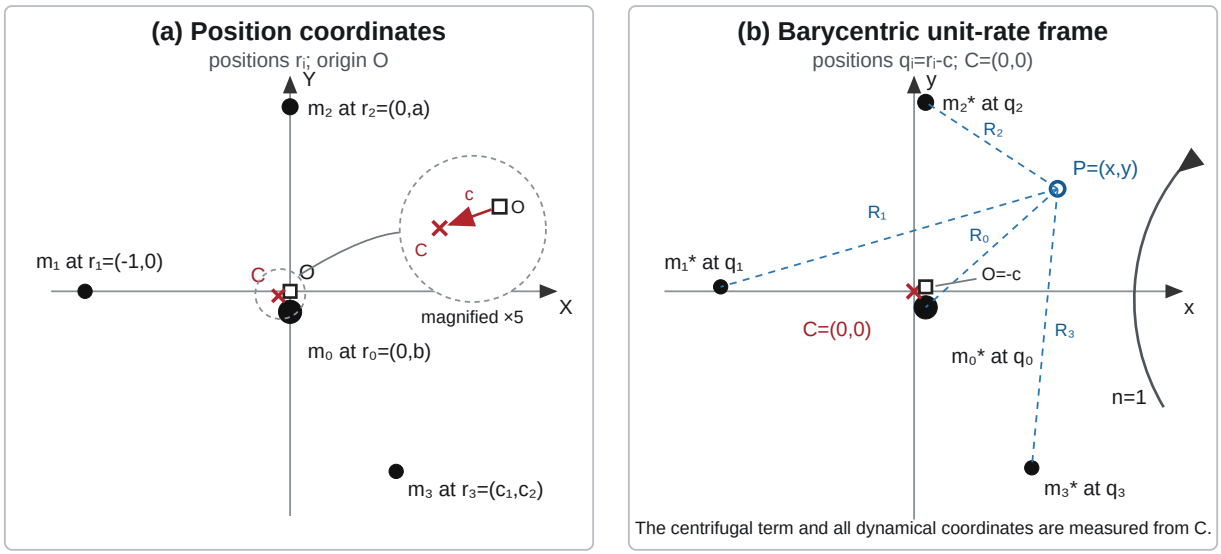


Figure 1: The two coordinate descriptions of the planar restricted $4+1$ body problem, drawn to scale for the Case-2 reference configuration. **(a)** The central-configuration formulae use the geometric positions $\mathbf{r}_i$ and geometric origin O; the inset enlarges the displacement $\mathbf{c}$ from O to the barycentre C. **(b)** The restricted dynamics use $\mathbf{q}_i = \mathbf{r}_i - \mathbf{c}$, so $C = (0, 0)$, the geometric origin is at $-\mathbf{c}$, and the fifth body $P = (x, y)$ is at the distances R_i from the primaries.

Let (x, y) be the barycentric rotating-frame position of the infinitesimal fifth body and define its primary distances by

$$R_i(x, y) = \sqrt{(x - q_{ix})^2 + (y - q_{iy})^2}, \qquad i = 0, \ldots, 3. \tag{19}$$

In the unit-angular-rate frame the effective potential is

$$\Omega(x, y) = \frac{1}{2}(x^2 + y^2) + \sum_{i=0}^{3} \frac{m_i^\star}{R_i}. \tag{20}$$

The centrifugal term, the primary coordinates and the fifth-body coordinates in (20) therefore use the same barycentric origin. Using the geometric positions $\mathbf{r}_i$ together with unit angular rate would mix the two coordinate descriptions and would not keep the primaries stationary in the assumed frame.

The equations of motion are

$$\ddot{x} - 2\dot{y} = \Omega_x, \qquad \ddot{y} + 2\dot{x} = \Omega_y, \tag{21}$$

where

$$\Omega_x = x - \sum_{i=0}^{3} m_i^\star \frac{x - q_{ix}}{R_i^3},$$
$$\Omega_y = y - \sum_{i=0}^{3} m_i^\star \frac{y - q_{iy}}{R_i^3}. \tag{22}$$

The restricted equilibria are precisely the stationary solutions

$$F(x, y; p) = \begin{pmatrix} \Omega_x \\ \Omega_y \end{pmatrix} = \mathbf{0}. \tag{23}$$

The primary points $R_i = 0$ are singularities and are excluded from the equilibrium domain.

2.3.1 Equilibrium bounds and derivatives

The equilibria are confined to a bounded region. Let

$$m_{\text{tot}} = \sum_{i=0}^{3} m_i^\star, \qquad d_{\max} = \max_i \|\mathbf{q}_i\|, \qquad r = \|(x, y)\|.$$

At an equilibrium with $r > d_{\max}$, (23) and the reverse triangle inequality give

$$r = \Big\| \sum_{i=0}^{3} m_i^\star \frac{(x, y) - \mathbf{q}_i}{R_i^3} \Big\| \le \frac{m_{\text{tot}}}{(r - d_{\max})^2},$$

so every equilibrium satisfies

$$r\,(r - d_{\max})^2 \le m_{\text{tot}}. \tag{24}$$

The left-hand side is strictly increasing for $r > d_{\max}$; hence no equilibrium lies outside the disk of radius R_{b}, where $R_{\text{b}} > d_{\max}$ is the unique root of

$$R_{\text{b}}\,(R_{\text{b}} - d_{\max})^2 = m_{\text{tot}}. \tag{25}$$

Writing

$$\Delta x_i = x - q_{ix}, \qquad \Delta y_i = y - q_{iy},$$

the Hessian entries are

$$\Omega_{xx} = 1 - \sum_{i=0}^{3} m_i^\star \left(\frac{1}{R_i^3} - \frac{3\Delta x_i^2}{R_i^5} \right),$$
$$\Omega_{yy} = 1 - \sum_{i=0}^{3} m_i^\star \left(\frac{1}{R_i^3} - \frac{3\Delta y_i^2}{R_i^5} \right),$$
$$\Omega_{xy} = 3 \sum_{i=0}^{3} m_i^\star \frac{\Delta x_i \Delta y_i}{R_i^5}. \tag{26}$$

Thus

$$H_\Omega = \begin{pmatrix} \Omega_{xx} & \Omega_{xy} \\ \Omega_{xy} & \Omega_{yy} \end{pmatrix} \tag{27}$$

is both the Hessian of Ω and the Jacobian of the equilibrium map. Consequently, $\det H_\Omega = 0$ is the local degeneracy condition used in the saddle-node analysis.

2.3.2 Jacobi integral and Hill regions

Equations (21) admit the Jacobi integral

$$C_J = 2\Omega(x, y) - \left(\dot{x}^2 + \dot{y}^2\right), \tag{28}$$

which is constant along each trajectory. Since the kinetic term is nonnegative, a trajectory at fixed C_J can visit only points satisfying

$$2\Omega(x, y) \geq C_J. \tag{29}$$

The corresponding allowed region and zero-velocity curve are

$$\mathcal{H}(C_J) = \{(x, y) : 2\Omega(x, y) \geq C_J\}, \tag{30}$$

$$2\Omega(x, y) = C_J. \tag{31}$$

At an equilibrium the rotating-frame velocity vanishes, and hence

$$C_{J,e} = 2\Omega(x_e, y_e). \tag{32}$$

The same invariant is used below to compare the critical levels of the equilibria with the Jacobi constants of the periodic families.

2.4 Equilibrium topology and linear stability

At an equilibrium (x_e, y_e), the first-order variational matrix is

$$A = \begin{pmatrix} 0 & 0 & 1 & 0 \\ 0 & 0 & 0 & 1 \\ \Omega_{xx} & \Omega_{xy} & 0 & 2 \\ \Omega_{xy} & \Omega_{yy} & -2 & 0 \end{pmatrix}_{(x_e, y_e)} . \tag{33}$$

Its characteristic polynomial has the invariant form

$$\lambda^4 + B\lambda^2 + C = 0, \qquad B = 4 - (\Omega_{xx} + \Omega_{yy}), \qquad C = \Omega_{xx}\Omega_{yy} - \Omega_{xy}^2 = \det H_\Omega. \tag{34}$$

Define

$$\Delta = B^2 - 4C. \tag{35}$$

The two roots in $z = \lambda^2$ are

$$z_\pm = \frac{-B \pm \sqrt{\Delta}}{2}.$$

Away from a collision, two purely imaginary conjugate pairs occur exactly when

$$B > 0, \qquad C > 0, \qquad \Delta > 0. \tag{36}$$

The boundary $\Delta = 0$, with $B, C > 0$, is treated separately as a repeated imaginary-eigenvalue collision. In a doubly-elliptic interval we write

$$\lambda = \pm i\omega_1, \qquad \lambda = \pm i\omega_2, \qquad \omega_{1,2}^2 = \frac{B \pm \sqrt{\Delta}}{2},$$

with the frequencies ordered explicitly whenever they are used to seed periodic families. These statements concern linear spectral stability only; they do not imply nonlinear or KAM stability.

The special form of the potential yields a global count constraint and a sharper local stability test. Set

$$S(x,y) = \sum_{i=0}^{3} \frac{m_i^\star}{R_i^3}. \tag{37}$$

Directly from (26),

$$\operatorname{tr} H_\Omega = \Delta_{x,y}\Omega = 2 + S > 0, \qquad B = 2 - S. \tag{38}$$

Theorem 1 (Morse count for four primaries)**.** *Fix four distinct primaries with positive normalised masses. Suppose that the restricted potential has finitely many equilibria and that every equilibrium is nondegenerate. If N_0 and N_1 denote the numbers of minima and saddles of Ω, respectively, then*

$$N_1 = N_0 + 3, \qquad N_{\mathrm{eq}} = N_0 + N_1 = 2N_0 + 3. \tag{39}$$

In particular, the total equilibrium count is odd.

Proof. The configuration domain is $\mathcal{D} = \mathbb{R}^2 \setminus \{\mathbf{q}_0, \dots, \mathbf{q}_3\}$. Since $\Omega \to +\infty$ at each puncture and as $\|(x,y)\| \to \infty$, $\Omega : \mathcal{D} \to \mathbb{R}$ is proper. Choose a regular value L above every critical value. Then the compact sublevel $K_L = \{\Omega \le L\}$ has the homotopy type of the four-punctured plane: equivalently, after truncating the outer end and the four puncture ends it is a disk with four open disks removed. Hence $\chi(K_L) = \chi(\mathcal{D}) = 1 - 4 = -3$. Equation (38) excludes negative-definite Hessians and hence local maxima. The Morse relation for K_L therefore reduces to $\chi(K_L) = N_0 - N_1 = -3$ [10], which gives (39). □

Remark 2. The argument uses only that $\Omega \to +\infty$ at each primary and at infinity and that Ω is subharmonic, so for n primaries it gives $N_1 = N_0 + (n-1)$. For $n = 2$ this is the circular restricted three-body problem, with the three collinear saddles and the two equilateral minima. For $n = 3$ it requires an even count, so the equilateral restricted four-body problem [2] can have eight or ten equilibria generically. Nine can occur only when at least one equilibrium is degenerate; under a generic one-parameter unfolding satisfying the usual transversality and nondegeneracy conditions, such a count transition occurs through a fold. For $n = 4$ the count is odd, as found below.

Corollary 3 (Analytic fold and spectral restrictions)**.** *At a generic equilibrium fold, the colliding pair consists of one minimum and one saddle, and the equilibrium count changes by two. Every saddle equilibrium is of saddle×centre spectral type. A minimum is doubly elliptic precisely when*

$$S < 2, \qquad 4 \det H_\Omega < (2 - S)^2. \tag{40}$$

Proof. At a simple fold, $\det H_\Omega = 0$ while $\operatorname{tr} H_\Omega > 0$, so the nonzero Hessian eigenvalue is positive. The generic local normal form therefore creates or destroys a minimum and a saddle. At a saddle, $C = \det H_\Omega < 0$; the two roots of the quadratic in $z = \lambda^2$ have opposite signs, giving one real and one imaginary pair. At a minimum, $C > 0$, and substituting $B = 2 - S$ into (36) gives (40). □

Condition (40) is the four-primary counterpart of the classical Gascheau–Routh criterion for the equilateral points of the circular restricted three-body problem [17, 9]. There $S \equiv 1$ at L_4 and L_5 for every mass ratio, so $B = 1$ identically and the stability boundary is reached when the second inequality fails, at the repeated frequency $\omega = 1/\sqrt{2}$. Here S is not constant along the equilibrium branches, so both inequalities are active and the boundary is located numerically in Section 4.

The two generic boundaries of a stable interval are dynamically distinct. If C reaches zero, the equilibrium is degenerate; it is a saddle-node fold when the null direction satisfies the transversality and nonzero-cubic conditions stated in Section 3.4. If instead Δ reaches zero while $B, C > 0$,

the two imaginary pairs coalesce. If a transverse parameter variation changes the sign of Δ from positive to negative, the colliding eigenvalues leave the imaginary axis as a complex quartet. In a two-degree-of-freedom Hamiltonian system such a departure requires the colliding pairs to have opposite Krein signatures [9]; equal-signature pairs pass through one another and remain on the axis. Such a transverse quartet-producing transition is therefore a linear Hamiltonian–Hopf collision. The corresponding nonlinear normal form is not computed in this paper.

3 Equilibrium bifurcation structure

The equilibrium calculations use the normalisation of Section 2 as the underlying four-primary central configuration is varied. The admissible central configurations are still determined by $\psi = 0$ together with positive mass ratios. For each admissible geometry, the restricted problem is constructed using the barycentric primary positions

$$\mathbf{q}_i = \mathbf{r}_i - \mathbf{c}$$

and the unit-rate masses

$$m_i^\star = \frac{\widehat{m}_i}{\kappa}.$$

Four reference configurations test the normalisation and equilibrium search. We continue the two admissible families containing Cases 1 and 2, determine the number of equilibrium points and identify the parameter values at which this number changes. The continuation coordinate is denoted by ℓ, with $s \in [0, 1]$ used as a normalised coordinate along each admissible component.

3.1 Reference configurations

We begin with the four reference configurations listed in Table 1. Since their quoted coordinates are given only to finite precision, each configuration is first refined to satisfy

$$\psi(a, b, c_1, c_2) = 0$$

with (a, b) fixed. The corresponding mass ratios are then recalculated from (7), and only positive, nonsingular configurations are retained.

For each refined configuration, the barycentre is calculated from (10) and the primary positions are translated to

$$\mathbf{q}_i = \mathbf{r}_i - \mathbf{c}.$$

The multiplier κ is then calculated from (14), and the unit-rate masses are obtained from

$$m_i^\star = \frac{\widehat{m}_i}{\kappa}.$$

As a final check on the normalisation, the unit-rate primary equations are evaluated directly at every configuration used in the restricted problem. We require

$$\mathcal{E}_{\mathrm{CC}} := \max_i \left\| \sum_{j \neq i} m_j^\star \frac{\mathbf{q}_j - \mathbf{q}_i}{|\mathbf{q}_j - \mathbf{q}_i|^3} + \mathbf{q}_i \right\| \leq 256\, \epsilon_{\mathrm{mach}} \max\left(1, \max_i |\mathbf{q}_i|\right), \tag{41}$$

together with the barycentric identity and agreement between the independent values of κ. These checks are satisfied throughout the calculations.

The equilibrium points are obtained by solving

$$F(x,y) = \begin{pmatrix} \Omega_x \\ \Omega_y \end{pmatrix} = \mathbf{0}$$

using a damped Newton method with the analytic Hessian H_Ω as Jacobian. To reduce the possibility of missing roots, each reference configuration is searched independently from a deterministic grid and from a large set of fixed-seed random initial points. The search domain contains the analytical bound R_b derived in (25).

The principal search uses an 81×81 grid together with 2000 random initial points. As an independent check, the calculations are repeated using a 161×161 grid and a separate 10000-start random search. All three searches recover the same equilibrium sets within the clustering tolerance. Converged Newton iterates separated by less than 10^{-6} in Euclidean position are identified as the same equilibrium. Accepted roots satisfy $\|\nabla\Omega\|_2 < 10^{-12}$ and are required to remain separated from the primary singularities. The analytic gradient and Hessian are also checked independently using central finite differences, with discrepancies of order 10^{-9}–10^{-10}.

Table 1 summarises the resulting normalisation and equilibrium counts. We obtain

$$N_\mathrm{eq} = 11,\ 9,\ 11,\ 9 \qquad \text{for Cases 1–4, respectively.} \tag{42}$$

The three independent searches return the same set of roots for each case. The largest equilibrium residual is of order 10^{-15}, and none of the accepted roots lies close to a primary singularity or a degenerate Hessian.

Table 1: Reference primary configurations. Geometric coordinates, κ, and the normalised masses are rounded to two decimal places for display. The quoted (c_1, c_2) values are the refined central-configuration geometries, κ is the multiplier of the representative mass vector $(\rho_0, \rho_1, \rho_2, 1)$, and N_eq is the equilibrium count in the barycentric unit-angular-rate restricted model.

Case	(a, b)	(c_1, c_2)	κ	$(m_0^\star, m_1^\star, m_2^\star, m_3^\star)$	N_0	N_1	N_eq
1	$(0.90, -0.10)$	$(-0.61,\ 0.72)$	53.74	$(0.92, 0.06, 0.02, 0.02)$	4	7	11
2	$(0.90, -0.10)$	$(\ 0.52, -0.88)$	5.33	$(0.80, 0.18, 0.24, 0.19)$	3	6	9
3	$(1.50,\ 0.40)$	$(-0.94,\ 1.00)$	3.34	$(0.90, 0.05, 0.13, 0.30)$	4	7	11
4	$(1.50,\ 0.40)$	$(\ 1.05,\ 0.13)$	3.77	$(1.14, 0.26, 0.19, 0.26)$	3	6	9

Cases 1 and 2 lie on the slice

$$(a, b) = (0.90, -0.10)$$

and will be continued throughout the remainder of the paper. Cases 3 and 4 lie on the second slice

$$(a, b) = (1.50, 0.40)$$

and are included as independent checks that the normalisation, equilibrium search and Morse relation behave consistently away from the main slice. In Case 3 the quoted value $c_2 = 1.00$ is rounded; the refined positive-mass configuration lies immediately before the boundary at which ρ_1 changes sign.

The variation in κ is substantial: the Case-1 value exceeds the Case-3 value by more than an order of magnitude. This confirms that the passage from mass ratios to a unit-rate restricted model is configuration-dependent and cannot be represented by one global common scaling factor. The

normalised masses also show that the two continued cases have very different mass distributions. Case 1 is strongly hierarchical, with $m_0^\star$ carrying about 90% of the total normalised mass, whereas the four masses in Case 2 are much more comparable.

Figure 2 displays the barycentric primary and equilibrium geometry for the two reference configurations on the continued slice. The local Morse counts shown in Table 1 satisfy $N_1 = N_0 + 3$ exactly, providing a direct numerical check of Theorem 1 for all four reference cases.

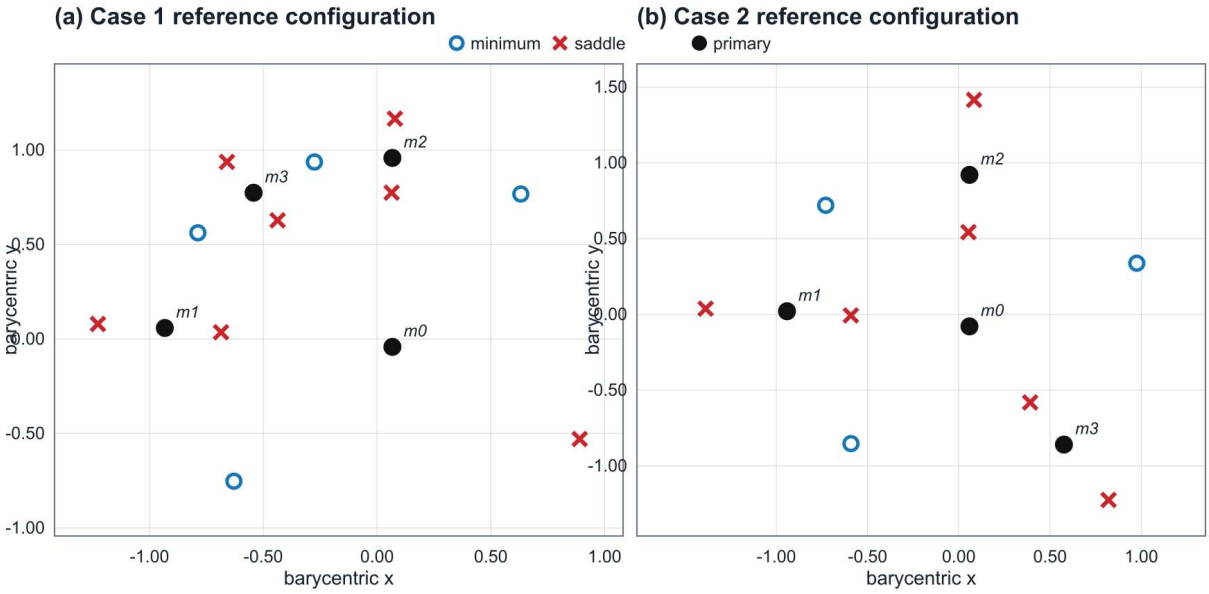


Figure 2: Barycentric equilibrium configurations for Cases 1 and 2. Open circles denote minima of Ω, crosses denote saddles, and black points denote the four primaries. Case 1 has four minima and seven saddles; Case 2 has three minima and six saddles.

3.2 Distinct admissible components on the fixed slice

Cases 1 and 2 lie on the same slice,

$$(a, b) = (0.90, -0.10),$$

and therefore provide a convenient setting in which to study how the admissible central configurations vary. With (a, b) fixed, we write

$$\mathbf{p} = (c_1, c_2)$$

and follow the level set

$$\psi(\mathbf{p}) = 0$$

by pseudo-arclength continuation [8, 1]. If $\mathbf{p}_k$ is an accepted point with unit tangent $\mathbf{t}_k$, the next point is obtained from the predictor-corrector system

$$\begin{cases} \psi(\mathbf{p}) = 0, \\ \mathbf{t}_k^T(\mathbf{p} - \mathbf{p}_k) - \Delta\ell = 0. \end{cases} \tag{43}$$

The step size is adjusted during the continuation, and each corrected point is required to remain in the positive-mass admissible region.

Before solving the restricted problem, each continuation point is refined locally onto $\psi = 0$ along the normal to the central-configuration curve. The mass ratios, barycentre, multiplier κ and unit-rate masses are then recalculated from the refined geometry. The equilibrium search is repeated independently at every continuation point; equilibria obtained at the preceding point are used only as additional initial estimates.

The continuation gives two qualitatively different regular components of $\psi = 0$ containing Cases 1 and 2. The component through Case 1 is an open branch, whereas the ambient curve through Case 2 closes numerically on itself. No zero of

$$\nabla_{(c_1,c_2)}\psi$$

is encountered along either continuation. Restricting the curves to positive masses produces two open admissible arcs containing Cases 1 and 2, respectively.

This conclusion applies only to the fixed slice $(a, b) = (0.90, -0.10)$. It does not imply that Cases 1 and 2 belong to different connected components of the full four-parameter admissible central-configuration set when a and b are also allowed to vary.

The mass ratios that vanish at the ends of the two arcs are also different. On the Case 1 arc,

$$\rho_0 \to 0 \quad (s \to 0), \qquad \rho_2 \to 0 \quad (s \to 1),$$

whereas on the Case 2 arc,

$$\rho_1 \to 0 \quad (s \to 0), \qquad \rho_0 \to 0 \quad (s \to 1).$$

In each limit, the remaining three massive primaries approach a three-body central configuration. The vanishing primary approaches an equilibrium of the restricted problem generated by these three primaries and therefore becomes, in the limit, a second massless body.

This limiting behaviour can also be seen in the restricted equilibria. For a small unit-rate mass $m_j^\star$, two equilibrium points occur near $\mathbf{q}_j$, at a distance of order

$$(m_j^\star)^{1/3},$$

and collapse onto $\mathbf{q}_j$ as $m_j^\star \to 0$. After their collapse the limiting three-primary problem has $N_{\mathrm{eq}} - 1$ equilibrium points, an even number in agreement with

$$N_1 = N_0 + 2$$

for three punctures.

For example, near the $s = 1$ endpoint of the Case 2 arc,

$$m_0^\star = 2.97 \times 10^{-4},$$

and exactly two equilibrium points lie within 0.04 of $\mathbf{q}_0$; the next nearest equilibrium is more than twenty times farther away. Thus the endpoints correspond to boundaries of the positive-mass admissible set and not to the saddle-node bifurcations identified below.

Figure 3 shows the two traced components in the (c_1, c_2) plane and locates the six restricted-equilibrium folds discussed below.

The discretised continuation consists of 116 points on the Case 1 arc and 113 points on the Case 2 arc. All 229 points are refined onto $\psi = 0$ before the restricted calculations are performed. The largest corrections are only

$$6.53 \times 10^{-14} \quad \text{and} \quad 1.80 \times 10^{-14},$$

respectively, and no point changes its ordering or admissibility. The maximum residual in the unit-rate primary equations is below 8×10^{-15}.

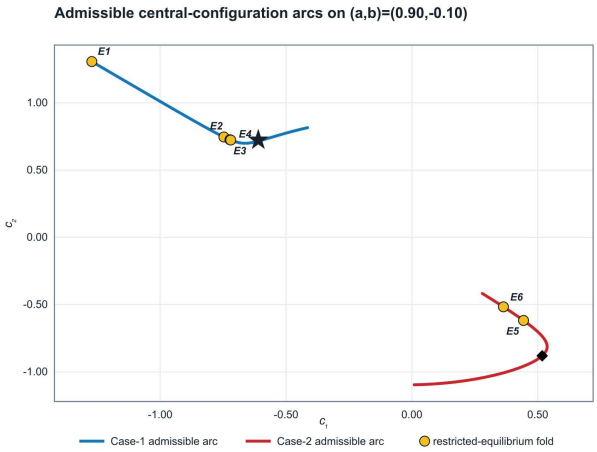


Figure 3: Admissible central-configuration components in the (c_1, c_2) plane on the fixed slice $(a, b) = (0.90, -0.10)$. The coloured curves are the positive-mass components containing Cases 1 and 2. The reference configurations are marked separately, and E1–E6 denote the six restricted-equilibrium saddle-node events encountered along these components.

3.3 Multiplicity cascades

At every projected continuation point the restricted equilibria are recomputed by an independent global multi-start search. The equilibrium-count sequences are

$$\boxed{\text{Case-1 arc: } 11 \to 13 \to 15 \to 13 \to 11} \tag{44}$$

and

$$\boxed{\text{Case-2 arc: } 9 \to 11 \to 9.} \tag{45}$$

Figure 4 shows the two multiplicity cascades and the locations of the six count-changing events. Accordingly,

$$N_{\text{eq}}^{\max} = 15 \tag{46}$$

is the largest multiplicity detected on the investigated slice.

Each sampled constant-count region is checked independently using a denser 161×161 grid and a separate 10000-start random search. These searches recover the same equilibrium sets. No sampled count change has magnitude other than two.

The first transition on the Case 1 arc occurs close to an admissible endpoint, but it is not caused by a vanishing primary mass. At the refined fold,

$$\rho_0 = 8.29 \times 10^{-3} > 0.$$

A separate solution of

$$\psi = \rho_0 = 0$$

locates the positive-mass boundary at a different primary configuration. Therefore the first pair of equilibria is created at an interior saddle-node while all four primary masses remain positive.

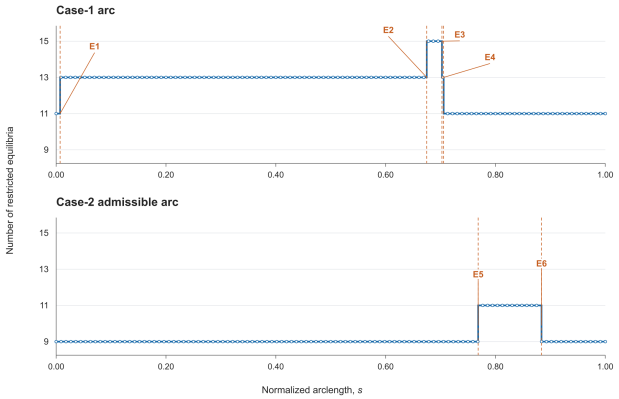


Figure 4: Restricted-equilibrium multiplicity along the two admissible central-configuration components on the fixed slice $(a, b) = (0.90, -0.10)$. The Case-1 arc follows $11 \to 13 \to 15 \to 13 \to 11$ through folds E1–E4, while the Case-2 arc follows $9 \to 11 \to 9$ through E5–E6. Counts at every continuation sample are obtained from independent global equilibrium searches in the barycentric unit-rate model.

3.4 Six nondegenerate saddle-node folds

Equilibrium points at neighbouring continuation steps are matched so that individual branches can be followed along the central-configuration curve. Near the first Case 1 fold, where three equilibria lie close together, the two branches created at the fold are continued locally and compared with the pre-existing branch. This removes the ambiguity in the branch assignment.

Whenever the equilibrium count changes between two neighbouring continuation points, the interval is narrowed by repeated bisection with a fresh equilibrium search at each step. The merging pair is then used to solve the augmented system

$$\mathcal{G}(x, y, c_1, c_2) = \begin{pmatrix} \Omega_x \\ \Omega_y \\ \det H_\Omega \\ \psi \end{pmatrix} = \mathbf{0}, \tag{47}$$

with (a, b) fixed. At each trial point the mass ratios, barycentre, multiplier κ and restricted potential are recalculated from the corresponding central configuration.

Let μ_0 be the Hessian eigenvalue that vanishes at the fold and let $\mu_\perp$ be the transverse eigenvalue. A simple saddle-node requires

$$\mu_0 = 0, \qquad \mu_\perp \neq 0,$$

together with

$$D^3\Omega[\mathbf{v}, \mathbf{v}, \mathbf{v}] \neq 0, \qquad \mathbf{v}^T F_\ell \neq 0, \tag{48}$$

where $\mathbf{v}$ is the normalised null direction. As a further numerical check, the separation d of the two equilibria on the side where the pair exists is fitted to

$$d \propto |\ell - \ell_c|^\gamma, \tag{49}$$

for which a generic saddle-node gives $\gamma = 1/2$.

Table 2: Locations and persistent branch identities of the six interior saddle-node folds. Restricted coordinates (x, y) are barycentric. The reporting coordinate s, the central-configuration coordinates (c_1, c_2), and the restricted coordinates (x, y) are rounded to two decimal places for display.

ID	Component	Change	Pair	s	c_1	c_2	x	y
E1	Case-1	$11 \to 13$	12,13	0.01	-1.27	1.31	0.75	-0.80
E2	Case-1	$13 \to 15$	14,15	0.67	-0.75	0.75	-0.33	0.32
E3	Case-1	$15 \to 13$	4,14	0.70	-0.72	0.73	-0.54	0.31
E4	Case-1	$13 \to 11$	5,12	0.71	-0.72	0.72	-0.20	0.62
E5	Case-2	$9 \to 11$	25,26	0.77	0.44	-0.62	-0.10	0.09
E6	Case-2	$11 \to 9$	19,26	0.88	0.36	-0.52	0.15	-0.25

Table 3: Numerical nondegeneracy checks for the six folds. Here μ_0 and $\mu_\perp$ are the null and transverse eigenvalues of H_Ω, $D^3\Omega[\mathbf{v}, \mathbf{v}, \mathbf{v}]$ is the third directional derivative along the unit null vector $\mathbf{v}$, $\mathbf{v}^T F_\ell$ is the parameter-transversality coefficient, γ is the fitted pair-separation exponent and $\|\mathcal{G}\|$ the residual of the augmented system (47). The signs of the directional coefficients depend on the chosen null-vector orientation; their nonzero magnitudes are the relevant tests.

ID	μ_0	$\mu_\perp$	$D^3\Omega[\mathbf{v}, \mathbf{v}, \mathbf{v}]$	$\mathbf{v}^T F_\ell$	γ	$\|\mathcal{G}\|$
E1	-5.57×10^{-14}	6.15	5.43	-0.62	0.50	3.43×10^{-13}
E2	4.22×10^{-15}	6.55	8.21	-1.12	0.50	2.79×10^{-14}
E3	-9.63×10^{-15}	6.70	-17.38	-3.34	0.50	6.41×10^{-14}
E4	9.10×10^{-15}	6.71	19.85	3.14	0.50	6.11×10^{-14}
E5	2.98×10^{-14}	8.34	28.46	-5.24	0.50	2.50×10^{-13}
E6	-2.60×10^{-13}	9.93	-31.49	-1.64	0.50	2.58×10^{-12}

At all six events, the null Hessian eigenvalue is at numerical solution tolerance while $\mu_\perp$ remains clearly nonzero. The two nondegeneracy coefficients are also well separated from zero. Independent searches on opposite sides of the folds reproduce the count changes

$$11 \to 13, \quad 13 \to 15, \quad 15 \to 13, \quad 13 \to 11, \quad 9 \to 11, \quad 11 \to 9.$$

The branch identities in Table 2 account for every creation and annihilation event: branch 8 survives the E1 interval, branch 12 exists only between E1 and E4, and E3 and E4 involve different merging pairs.

For all six folds, the fitted exponent is close to the expected value $1/2$; the largest deviation is 3.04×10^{-3}. This square-root behaviour provides an additional numerical check of the saddle-node classification. The minimum–saddle character and the change in equilibrium count by two follow independently from Corollary 3.

The two Case 1 annihilation events E3 and E4 occur very close together in the primary configuration space,

$$\Delta s = 3.14 \times 10^{-3}, \qquad \|\Delta(c_1, c_2)\| = 3.61 \times 10^{-3},$$

but their restricted fold locations are separated by approximately 0.46 and they involve different equilibrium pairs. Their separation and branch identities establish two distinct simple folds.

4 Stability and centre modes

The invariants B, C and Δ of (34)–(35) determine the linear spectrum of the equilibrium branches obtained in Section 3. By Corollary 3, every saddle of Ω is saddle×centre, while spectral stability is

possible only at a minimum. For a minimum the criterion is given by (40).

The eigenvalues are also computed directly from the full variational matrix (33) as an independent numerical check. Non-fold zeros of Δ are refined along the corresponding equilibrium branches, and the sign change of Δ is used to distinguish the local spectral transition.

The notation H1 is reserved for the 1:1 imaginary-eigenvalue collision identified below. The periodic families H1a and H1b introduced in Section 5 are finite-amplitude families continued from a nearby parent equilibrium and should not be confused with the linear collision itself.

4.1 Spectral classes and the Case-2 stability boundary

The continuation contains 2485 equilibrium samples on the 26 tracked branches of Table 2. The two primary-configuration components have markedly different spectral structures. None of the 1444 sampled equilibria on the Case 1 arc is spectrally stable: 896 are saddle×centre, 547 have a complex-quartet spectrum, and one has two real pairs. On the Case 2 arc, 17 of the 1041 sampled equilibria are spectrally stable, all on branch 24. The remaining samples comprise 690 saddle×centre equilibria and 334 complex quartets; no second stable branch is found.

The four reference configurations are also unstable. At each reference case, the N_1 saddles of Table 1 are saddle×centre, while all N_0 minima have a complex-quartet spectrum. Thus none of the reference configurations contains a doubly elliptic equilibrium.

Branch 24 is doubly elliptic from the admissible endpoint $s = 0$ to a non-fold spectral collision. Refinement of this transition gives

$$s_H = 0.14564, \qquad (c_1, c_2)_H = (0.17, -1.07), \tag{50}$$

with barycentric equilibrium

$$(x_H, y_H) = (0.99, 0.20). \tag{51}$$

The spectral invariants at the collision are

$$B_H = 0.99, \tag{52}$$

$$C_H = 0.25, \tag{53}$$

$$\Delta_H \simeq -3.3 \times 10^{-15}. \tag{54}$$

Since $B_H > 0$ and $C_H > 0$, the two imaginary pairs coalesce at

$$\omega_c = \sqrt{\frac{B_H}{2}} = 0.70, \tag{55}$$

so the limiting spectrum is the repeated pair $\lambda = \pm i\omega_c$.

The numerical values are close to those at the classical Routh boundary. By (38), $B_H = 0.99$ corresponds to

$$S = \sum_{i=0}^{3} \frac{m_i^\star}{R_i^3} = 1.01$$

at the transition, compared with $S \equiv 1$ at the equilateral points of the circular restricted three-body problem. The collision frequency $\omega_c = 0.70$ differs from the Routh value $1/\sqrt{2} = 0.71$ by about 0.3%, despite the strongly non-symmetric four-primary configuration.

The collision is transverse. Centred estimates at decreasing arclength steps converge to

$$\left.\frac{d\Delta}{d\ell}\right|_{H1} \simeq -3.20. \tag{56}$$

For $s < s_H$, we have $B, C, \Delta > 0$, and the two distinct positive frequencies approach one another as $s \to s_H^-$. On the high-s side of the collision, $\Delta < 0$ and the spectrum is a complex quartet. Figure 5 shows both the frequency collision and the transverse zero of Δ.

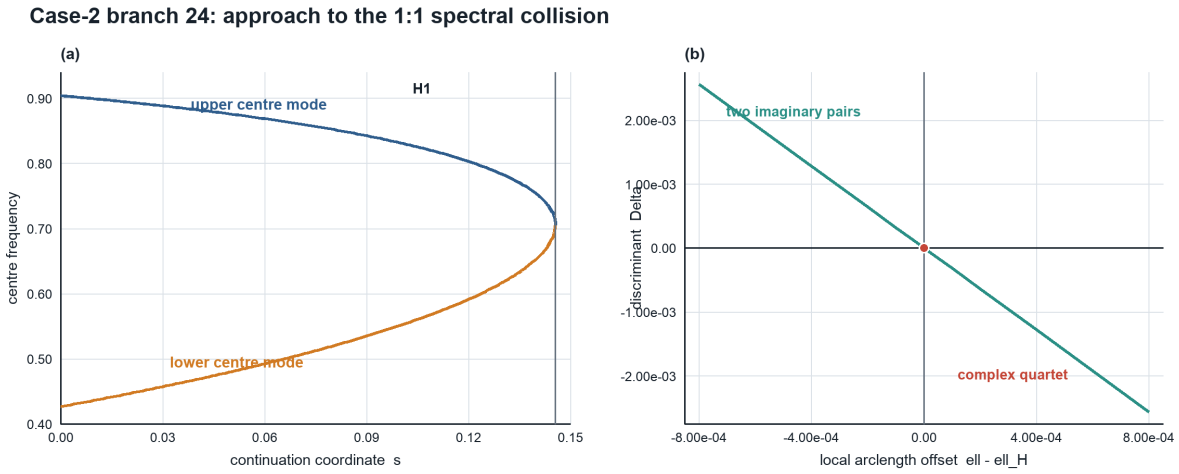


Figure 5: The stability boundary on Case-2 branch 24. (a) The two positive imaginary frequencies coalesce at H1. (b) A local arclength calculation shows the transverse sign change of Δ, from two imaginary pairs to a complex quartet.

The observed sequence is therefore

$$\text{two imaginary pairs} \longrightarrow \text{repeated imaginary pair} \longrightarrow \text{complex quartet}.$$

Thus H1 is a transverse linear Hamiltonian–Hopf spectral transition at a 1:1 imaginary-eigenvalue collision. As noted after Corollary 3, departure from the imaginary axis requires opposite Krein signatures, that is, opposite energy signatures of the colliding Hamiltonian modes. The observed departure as a complex quartet therefore implies this signature configuration. This classification is linear; no nonlinear normal form or nonlinear stability analysis is used here. The strictly stable interval is

$$\boxed{0 \le s < s_H, \qquad s_H = 0.14564.} \tag{57}$$

At $s = s_H$, the repeated imaginary pair is marginal and forms the boundary of the stable interval.

4.2 A real-axis collision on Case 1

A second non-fold zero of Δ occurs on Case-1 branch 12 at

$$s_R = 0.01, \qquad (c_1, c_2)_R = (-1.27, 1.30), \tag{58}$$

with barycentric equilibrium

$$(x_R, y_R) = (0.73, -0.79).$$

At this event,

$$B_R = -2.20, \qquad C_R = 1.21, \qquad \Delta_R \simeq 2.9 \times 10^{-12}.$$

Since $B_R < 0$, the repeated collision lies on the real axis, with

$$\lambda_c^2 = -\frac{B_R}{2} > 0, \qquad |\lambda_c| = 1.05. \tag{59}$$

The local sequence is

$$\text{two real pairs} \longrightarrow \text{repeated real pair} \longrightarrow \text{complex quartet},$$

with

$$\left.\frac{d\Delta}{d\ell}\right|_{R1} \simeq -756.0.$$

Both sides are unstable, so R1 changes only the type of instability. The contrast with H1 shows that the condition $\Delta = 0$ alone does not classify a collision: both H1 and R1 are transverse zeros of Δ, but the signs of B and C place one on the imaginary axis and the other on the real axis. Other sampled sign changes of B also remain within unstable spectral classes. No non-fold $C = 0$ event is detected; the only sampled zeros of C are the six saddle-node folds.

4.3 Numerical validation and centre modes

Across all 2485 equilibrium samples, the eigenvalues obtained from the full matrix (33) and from the quartic (34) agree to a maximum absolute discrepancy of

$$1.24 \times 10^{-14}.$$

The maximum defect in the Hamiltonian spectral symmetry $\lambda \mapsto -\lambda, \bar{\lambda}, -\bar{\lambda}$ is 1.14×10^{-14}. At E1–E6, the expected zero pair is recovered; the larger matching sensitivity there is consistent with the conditioning of a polynomial near a multiple root.

The spectral map also determines the available Lyapunov-centre seeds. A saddle×centre equilibrium contains one simple imaginary pair, but the hyperbolic companion direction makes the parent equilibrium unstable. A complex quartet supplies no imaginary centre pair. On the investigated fixed-(a, b) slice, the finite doubly elliptic interval on Case-2 branch 24 is the only resolved source of two distinct centre modes from a spectrally stable equilibrium. The periodic families in the next section are chosen to compare these two modes with the single centre mode of a saddle×centre parent.

5 Periodic-orbit families

We continue five representative Lyapunov families from the centre modes identified in Section 4.3. Families G1 and G2 arise from the two centre modes of a well-separated doubly elliptic equilibrium, H1a and H1b from the two centre modes of an equilibrium close to the 1:1 boundary H1, and S1 from the single centre mode of a saddle×centre equilibrium. These continuations are used to compare the three dynamical settings and are not intended as maximal global families. In particular, Floquet degeneracies are identified below without assigning a nonlinear branch type.

The generic doubly elliptic parent lies on Case-2 branch 24 at $s = 0.06$, where

$$(\omega_1, \omega_2) = (0.87,\ 0.50), \qquad \frac{\omega_1}{\omega_2} = 1.75.$$

The near-H1 parent lies on the same branch at $s = 0.14$, with

$$(\omega_1, \omega_2) = (0.75,\ 0.65), \qquad \frac{\omega_1}{\omega_2} = 1.16.$$

The saddle×centre parent is chosen on Case-1 branch 9 at $s = 0.85$, with centre frequency $\omega_c = 1.04$ and real hyperbolic pair $\lambda = \pm 0.37$.

5.1 Periodic families and shooting formulation

Write the rotating-frame state as

$$\mathbf{u} = (x, y, \dot{x}, \dot{y})^T$$

and denote the time-T flow by $\phi_T(\mathbf{u}_0)$. A periodic orbit satisfies

$$\phi_T(\mathbf{u}_0) - \mathbf{u}_0 = \mathbf{0}. \tag{60}$$

Let $L = (x^*, y^*, 0, 0)^T$ be a parent equilibrium with simple centre eigenvalue $+i\omega_k$ and eigenvector $\mathbf{w}_k$. After fixing the eigenvector phase, the linear seed is

$$\mathbf{u}_0^{(0)} = L + \varepsilon \widehat{\mathbf{e}}_k, \qquad \widehat{\mathbf{e}}_k = \frac{\operatorname{Re} \mathbf{w}_k}{\| \operatorname{Re} \mathbf{w}_k \|}, \qquad T_0 = \frac{2\pi}{\omega_k}. \tag{61}$$

At a doubly elliptic parent the two simple centre modes are seeded independently.

The full-period corrector uses the closure equations (60) together with the phase and amplitude conditions

$$\widehat{\mathbf{e}}_k^T f(\mathbf{u}_0) = 0, \qquad \widehat{\mathbf{e}}_k^T (\mathbf{u}_0 - L) = a. \tag{62}$$

Thus

$$\mathcal{R}(\mathbf{u}_0, T) = \begin{pmatrix} \phi_T(\mathbf{u}_0) - \mathbf{u}_0 \\ \widehat{\mathbf{e}}_k^T f(\mathbf{u}_0) \\ \widehat{\mathbf{e}}_k^T (\mathbf{u}_0 - L) - a \end{pmatrix}. \tag{63}$$

This gives six scalar residuals for the five unknowns $(\mathbf{u}_0, T)$. One closure equation is locally redundant at a periodic solution because the autonomous flow preserves the Jacobi integral. The phase condition removes the time-shift freedom, while the amplitude condition selects one member of the family. No assumption that $\mathcal{M} - I$ has a two-dimensional geometric kernel is required; the trivial multiplier $+1$ may have a generalized eigenvector.

The state-transition matrix satisfies

$$\dot{\Phi} = A(\mathbf{u}(t))\Phi, \qquad \Phi(0) = I,$$

with monodromy matrix $\mathcal{M} = \Phi(T)$. The Newton–least-squares Jacobian is

$$J = \begin{pmatrix} \mathcal{M} - I & f(\phi_T(\mathbf{u}_0)) \\ \widehat{\mathbf{e}}_k^T A(\mathbf{u}_0) & 0 \\ \widehat{\mathbf{e}}_k^T & 0 \end{pmatrix}. \tag{64}$$

The five families are first continued at fixed amplitude. H1a and H1b are then extended independently by adding a secant pseudo-arclength condition to (63).

5.2 Lyapunov limit and family geometry

All state and variational integrations use DOP853, an adaptive explicit eighth-order Runge–Kutta method, with

$$\text{rtol} = \text{atol} = 10^{-12}.$$

The implementation was checked against an independently written formulation of the same equations at the level of the potential, gradient, Hessian, vector field, Jacobi integral and variational equations. The maximum Hessian/variational-matrix discrepancy is 3.55×10^{-15}; re-integration of a benchmark orbit gives final-state and monodromy differences of 2.25×10^{-14} and 2.08×10^{-13}, respectively. A

directional finite-difference test of the state-transition matrix gives a maximum relative error of 2.21×10^{-9}, while non-periodic trajectories conserve the Jacobi integral to 1.13×10^{-12}.

Before finite-amplitude continuation, each selected mode is computed at amplitudes

$$2 \times 10^{-4}, \qquad 5 \times 10^{-4}, \qquad 10^{-3}, \qquad 2 \times 10^{-3}.$$

For the smallest members, the periods converge to the linear values $2\pi/\omega_k$ as shown in Table 4. The initial-state displacement also scales linearly with the prescribed seed amplitude. In particular, H1a and H1b converge separately to $2\pi/\omega_1$ and $2\pi/\omega_2$, confirming that they arise from the two distinct near-H1 centre modes.

Table 4: Relative period error at the smallest computed member of each family.

Family	G1	G2	H1a	H1b	S1
$\lvert T - T_0\rvert/T_0$	4.27×10^{-9}	7.85×10^{-9}	3.91×10^{-9}	2.51×10^{-8}	3.36×10^{-10}

Figure 6 compares the first and largest fixed-amplitude members of the five families. G1 and G2 develop from the same parent through geometrically distinct centre modes. H1a and H1b remain smaller over this continuation interval, while S1 occupies a separate region around its Case-1 parent.

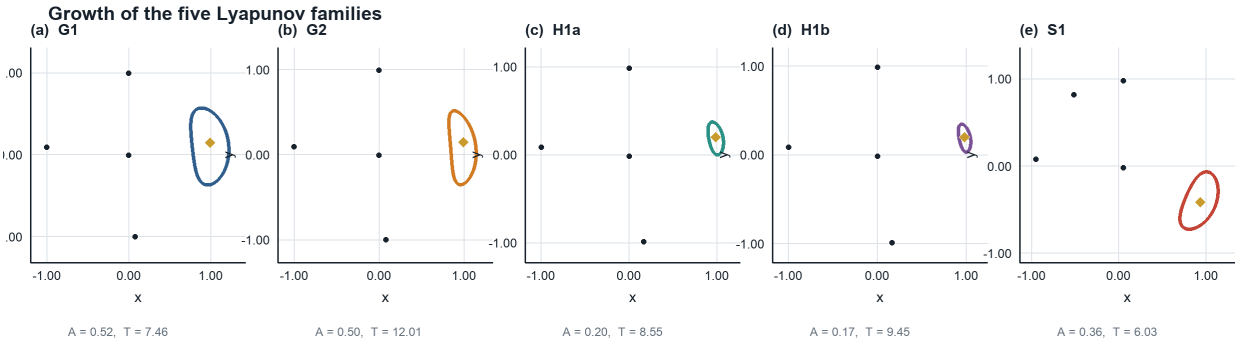


Figure 6: Representative configuration-space projections of the five Lyapunov families. The faint curve is the first computed member and the saturated curve is the largest fixed-amplitude member. Black circles mark the primaries and the gold diamond marks the parent equilibrium. Each panel uses its own equal coordinate scale; the largest member's amplitude and period are given below the panel.

5.3 Floquet stability of the five families

The Floquet multipliers are the eigenvalues of $\mathcal{M} = \Phi(T)$. For a periodic orbit of this autonomous Jacobi-integrable system, the monodromy matrix has the trivial multiplier pair $+1, +1$. After removing this pair, the remaining reciprocal pair λ, λ^{-1} is described by

$$\nu = \lambda + \lambda^{-1}. \tag{65}$$

For $|\nu| < 2$ the nontrivial pair lies on the unit circle, whereas $|\nu| > 2$ gives a real reciprocal instability. The values $\nu = +2$ and $\nu = -2$ correspond to collisions at $+1$ and -1, respectively. Here "Floquet

stable" refers only to the linear periodic-orbit spectrum; it is distinct from the spectral stability of the parent equilibrium and does not imply nonlinear or KAM stability.

For

$$A = \max_t \|(x(t), y(t)) - (x^*, y^*)\|,$$

Table 5 gives the fixed-amplitude continuation ranges. The near-H1 families are extended beyond these ranges in the next subsection.

Table 5: Fixed-amplitude periodic families. Jacobi ranges are given in Table 10.

Family	N	$A_{\max}$	$T_{\min}$	$T_{\max}$	Nontrivial Floquet pair
G1	26	0.52	7.24	7.46	unit circle
G2	26	0.50	12.01	12.69	unit circle
H1a	26	0.20	8.33	8.55	unit circle
H1b	25	0.17	9.45	9.64	unit circle
S1	25	0.36	6.03	6.03	real reciprocal

Across these 128 solutions, the closure residual is below 8.30×10^{-11}, the phase residual below 1.90×10^{-13}, and the maximum Jacobi variation 2.20×10^{-13}. G1 and G2 retain a unit-circle nontrivial pair over their computed ranges. S1 is Floquet unstable throughout, with a real reciprocal nontrivial pair. The corresponding changes in T, C_J and ν are shown in Figure 7.

The two families seeded at a common parent leave the parent critical Jacobi level in opposite directions. The common values are $C_{J,e}^{(24)} = 3.11$ for G1/G2 and 3.13 for H1a/H1b. The associated Hill-region changes are discussed in Section 6.

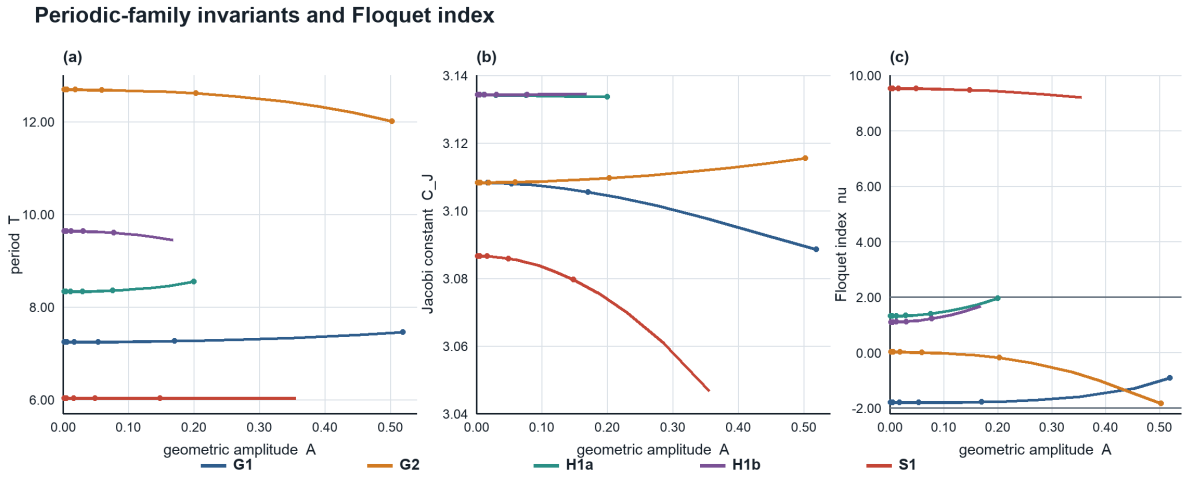


Figure 7: Period, Jacobi constant and nontrivial Floquet index along the five fixed-amplitude families. The horizontal lines at $\nu = \pm 2$ mark the boundaries of the unit-circle interval. The large positive index of S1 shows its real reciprocal instability.

5.4 Near-H1 families and finite-amplitude +1 degeneracies

Because the two parent frequencies lie close to the equilibrium 1:1 collision, H1a and H1b are continued independently with small pseudo-arclength steps. Overlap calculations reproduce four fixed-amplitude members with maximum state and period differences of 1.73×10^{-10} and 9.80×10^{-11}, respectively, confirming that the two continuations remain on their intended families.

Each family reaches a distinct nontrivial +1 Floquet-multiplier degeneracy. The refined events are listed in Table 6, and Figure 8 shows the separate crossings.

Table 6: Refined finite-amplitude +1 degeneracies on the near-H1 families. The coordinate ℓ is the family pseudo-arclength and $\delta C_J = C_J - C_{J,e}^{(24)}$ is measured from the parent's critical level; the two events lie on opposite sides of it.

Family	ℓ	A	T	$10^3\,\delta C_J$	$d\nu/d\ell$
H1a	0.01	0.20	8.56	−0.52	2.33
H1b	0.13	0.21	9.32	+0.43	2.19

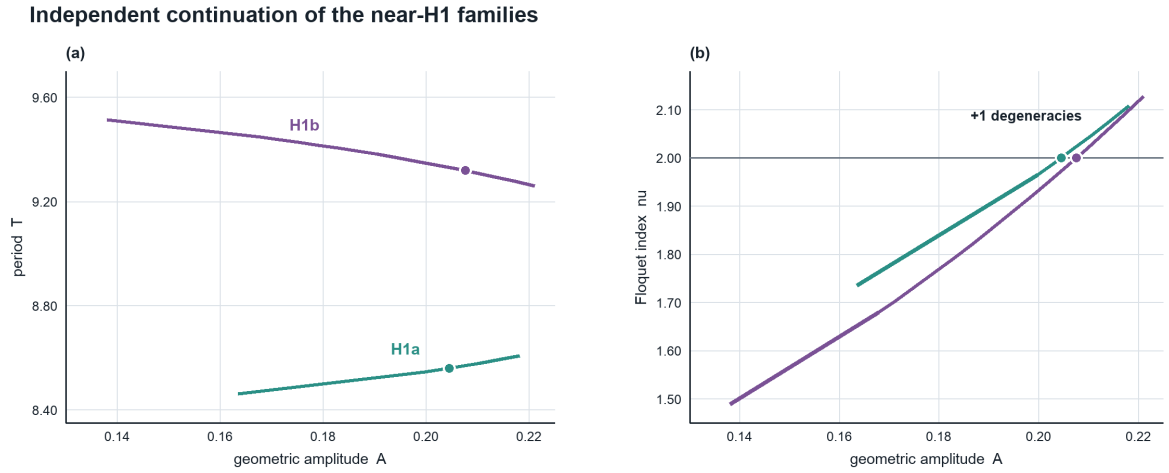


Figure 8: Independent pseudo-arclength continuation of H1a and H1b. The periods remain well separated while both nontrivial Floquet indices cross $\nu = 2$. Filled circles mark the independently refined +1 events.

The event-state brackets have widths 4.63×10^{-11} for H1a and 2.94×10^{-11} for H1b. Centred differences at decreasing steps give nonzero limiting values of $d\nu/d\ell$, so both crossings are transverse. To compare the two closed trajectories independently of their arbitrary time origins, the state-space separation is minimised over a relative phase shift. Their geometric separation in configuration space is measured by the symmetric Hausdorff distance between the sampled closed curves. With these definitions, the phase-optimised state separation is 8.09×10^{-3} and the orbit Hausdorff distance is 4.26×10^{-3}; their periods differ by 0.76, and their Jacobi constants by 9.44×10^{-4}.

Near an all-+1 spectrum, individually sorted characteristic roots are ill-conditioned. The degeneracies are therefore assessed mainly through invariant quantities. At the tightest integration tolerance, the trace- and pair-index defects from +2 are 4.80×10^{-10} and 4.91×10^{-7} for H1a, with

closure 8.76×10^{-14}; for H1b they are 7.80×10^{-10} and 8.80×10^{-7}, with closure 4.79×10^{-13}. The trace, determinant, reciprocal pairing, Jacobi variation and characteristic-polynomial coefficients converge more strongly than the individual multipliers. These calculations identify two distinct transverse periodic-orbit +1 Floquet-multiplier degeneracies to the resolved numerical accuracy. They do not, without additional nonlinear bifurcation analysis, distinguish a pitchfork, transcritical, saddle-node or family-reconnection event.

The Jacobi constant also has an extremum at each event to the resolved accuracy. Local quadratic fits give $dC_J/d\ell = 1.98 \times 10^{-7}$ and $d^2C_J/d\ell^2 = 1.19 \times 10^{-2}$ at H1a, and $dC_J/d\ell = 1.38 \times 10^{-6}$ and $d^2C_J/d\ell^2 = -7.03 \times 10^{-3}$ at H1b. Thus each event is a nondegenerate extremum of the projection of its periodic family onto C_J. This still does not determine the branch interaction in the full shooting variables; that would require branch switching or an equivalent nonlinear analysis.

These finite-amplitude degeneracies occur along nonlinear Lyapunov families at a fixed parent configuration and are distinct from the equilibrium collision H1 of Section 4.1. Their proximity to H1 is therefore suggestive, but does not by itself establish a common nonlinear bifurcation mechanism.

5.5 Rosette-type circulating periodic families from resonant Kepler seeds

The Lyapunov families considered above are local families generated by centre modes of an equilibrium. The large circulating periodic orbits considered here wind around the primary system on rosette-type trajectories. The same Case-2 branch 24 configuration at $s = 0.0621305662$ supports this different class of periodic motion. This is favoured by the strongly hierarchical unit-rate masses

$$M^* = (0.974998,\ 0.005693,\ 0.057619,\ 0.046515),$$

for which the dominant primary lies only 0.0113 from the barycentre and the other three primaries lie close to radius one. In this configuration the motion sufficiently far inside or outside the outer-primary ring is therefore well approximated initially by a Kepler orbit about the dominant mass.

We use commensurate Kepler orbits only as seeds. If the Kepler mean motion is $n = p/q$ for a prograde seed, the corresponding orbit closes in the unit-rate rotating frame after $T = 2\pi q$ in the unperturbed limit. The labels Pp:q used below refer to this seed construction; the lobe count and winding number quoted for the final solutions are measured from the converged trajectories and are not imposed by the label.

The equilibrium-based phase and amplitude conditions in (62) are replaced by an apsis condition and a fixed initial radius. With $\mathbf{u}_0 = (x_0, y_0, \dot{x}_0, \dot{y}_0)^T$, the corrector solves

$$\mathcal{R}_c(\mathbf{u}_0, T) = \begin{pmatrix} \phi_T(\mathbf{u}_0) - \mathbf{u}_0 \\ x_0\dot{x}_0 + y_0\dot{y}_0 \\ \sqrt{x_0^2 + y_0^2} - R \end{pmatrix} = \mathbf{0}. \tag{66}$$

As in (63), this gives six scalar residuals for five unknowns. The apsis condition removes the time-shift freedom, while R selects one member of the family and is subsequently used as the continuation parameter.

A direct correction of a Kepler seed in the full four-primary model is not reliable because the light primaries produce appreciable apsidal precession. The periodic orbit is therefore reached through a two-stage homotopy. First, the three light primary masses are restored continuously from zero to their physical values while the dominant primary is held at the origin. The dominant primary is then moved from the origin to its true barycentric position. At the starting point the problem is the rotating Kepler problem, where the seed is known explicitly; only the endpoint of the

homotopy is used as a physical solution of the restricted five-body model. Each stage is corrected by Levenberg–Marquardt least squares. The damping term regularises the correction when the shooting Jacobian becomes poorly conditioned. All integrations use DOP853 with rtol = atol = 10^{-12}.

Three circulating families were obtained in this way. Their generating members are listed in Table 7. P1:2 is an exterior orbit enclosing the four-primary system, whereas P2:1 and P3:1 are interior orbits around the dominant primary. The measured winding numbers are -1, $+1$ and $+2$, respectively. The nontrivial Floquet index shows that the P1:2 generating orbit is unstable with a real reciprocal multiplier pair, while the P2:1 and P3:1 generating orbits have their nontrivial pair on the unit circle.

Table 7: Generating members of the three circulating periodic families at the Case-2 branch 24 configuration with $s = 0.0621305662$. The lobe count and winding number are measured from the converged rotating-frame trajectory; ν is the nontrivial Floquet index of (65).

Family	T	C_J	Lobes	Winding	ν	Floquet type
P1:2	11.58238	3.34963	1	-1	-4.128	real reciprocal
P2:1	5.20895	3.33440	2	$+1$	-1.091	unit circle
P3:1	6.86566	3.58743	3	$+2$	$+1.974$	unit circle

The three families contain 13, 21 and 14 accepted members, respectively. Over all 48 continued solutions the closure residual remains below 8.75×10^{-11} and the Jacobi variation below 5.95×10^{-12}. Family continuation is stopped if the closure or Jacobi checks fail or if the distance to a primary falls below the prescribed near-collision gate. Figure 9 shows the resulting families in the rotating frame.

These solutions show that the periodic dynamics of the model are not confined to local Lyapunov families near equilibria. At the same primary configuration, large-scale circulating periodic motion coexists with the local families, and the three families display different Floquet character.

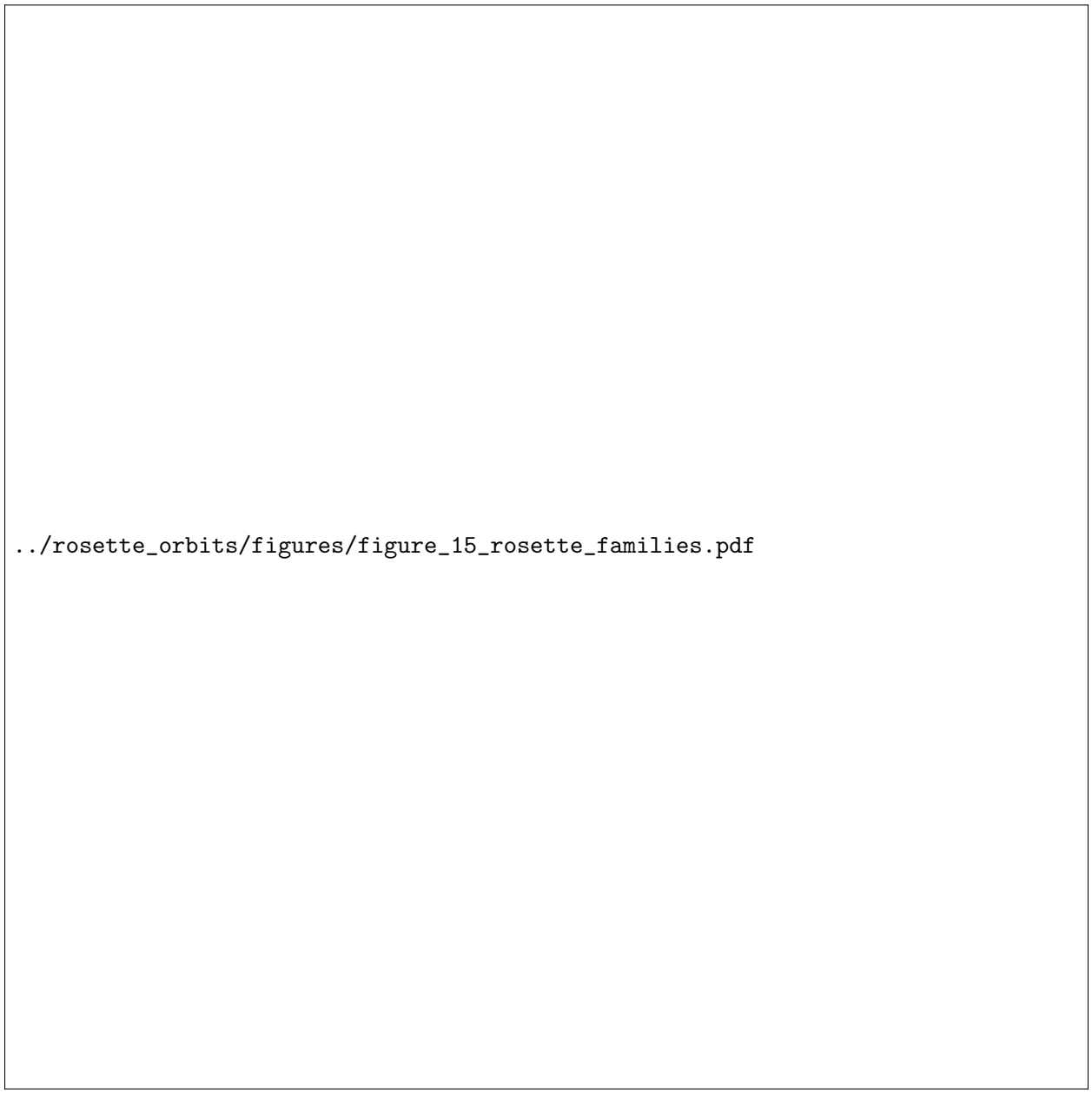


Figure 9: Rosette-type circulating periodic families at the Case-2 branch 24 configuration. Panel (a) shows the three families on one common coordinate scale, while panels (b)–(d) show P1:2, P2:1 and P3:1 separately with equal coordinate scales. Black circles mark the four primaries. Each curve is a separately converged periodic orbit of the full four-primary model, and shading follows the continuation in the initial-radius constraint. P1:2 forms an exterior one-lobed family with winding -1; P2:1 and P3:1 are interior two- and three-lobed families with winding $+1$ and $+2$, respectively.

6 Jacobi levels and Hill-region topology

The Jacobi integral gives a geometric description of the equilibrium and periodic-orbit results through the allowed region $\mathcal{H}(C_J)$ and the zero-velocity curve of (30)–(31). Since $2\Omega \to +\infty$ both at each primary and as $r = \sqrt{x^2 + y^2} \to \infty$, every finite Jacobi level contains an unbounded exterior allowed component together with allowed punctured neighbourhoods of the four primaries. Depending on C_J, these five regions may remain separate or become connected through equilibrium necks.

The equilibria are precisely the critical points of Ω. Hence the topology of a regular Hill region can change only when C_J crosses a critical value

$$C_{J,e}^{(i)} = 2\Omega(L_i), \tag{67}$$

where i denotes the equilibrium branch. Along the two primary-configuration arcs, the critical levels satisfy

$$3.00 \le C_{J,e} \le 6.46 \quad \text{(Case-1 arc)},$$

and

$$3.09 \le C_{J,e} \le 7.02 \quad \text{(Case-2 arc)}.$$

These ranges are obtained from all 2485 tracked equilibrium samples, using the persistent branch identities of Sections 3 and 4.

6.1 Critical Jacobi levels at the selected configurations

Table 8 gives the descending critical-level ladder at the two reference configurations and at the three periodic-orbit parents. Each equilibrium is refined before its Jacobi level is evaluated and ordered. The 49 critical points comprise 32 saddles and 17 minima of Ω; no maximum occurs. The closest pair is found at the saddle×centre parent, where branches 6 and 1 differ by 2.33×10^{-3}, so the numerical ordering remains resolved.

Table 8: Equilibrium critical Jacobi levels $C_{J,e} = 2\Omega(L_i)$ at the two reference configurations and the three periodic-orbit parents, listed by descending rank k. Each entry gives the equilibrium branch (br.) and its level. Three decimals are retained because the displayed ordering is the content of the table and the closest pair differs by 2.33×10^{-3}. An asterisk marks a minimum of Ω; the remaining branches are saddles.

k	Case 1		Case 2		G1/G2 parent		H1a/H1b parent		S1 parent	
	br.	$C_{J,e}$	br.	$C_{J,e}$	br.	$C_{J,e}$	br.	$C_{J,e}$	br.	$C_{J,e}$
1	8	3.463	22	4.835	20	3.669	20	3.756	8	3.424
2	3	3.389	20	4.715	22	3.633	22	3.718	3	3.362
3	13	3.257	23	4.569	21	3.592	21	3.664	15	3.175
4	11	3.230	19	4.508	23	3.570	23	3.644	13	3.168
5	15	3.220	21	4.421	19	3.232	19	3.352	2	3.161
6	2	3.199	16	4.294	16	3.224	16	3.334	11	3.155
7	9	3.109	18*	3.744	18*	3.130	18*	3.170	9	3.087
8	6*	3.085	17*	3.621	17*	3.127	17*	3.161	6*	3.056
9	1*	3.082	24*	3.582	24*	3.108	24*	3.134	1*	3.054
10	10*	3.033							10*	3.028
11	7*	2.999							7*	2.996

The local change at each critical level follows from the Morse lemma. At a saddle, the Hessian has one positive and one negative eigenvalue, and lowering C_J through $C_{J,e}$ opens a neck in the

superlevel set. This neck may join two allowed components, connect an interior allowed component to the exterior, or change the connectivity of the forbidden set. At a minimum, both Hessian eigenvalues are positive and lowering C_J closes a bounded forbidden component. These local changes are constrained by Theorem 1; the global attachment pattern is determined from the connected components of the allowed and forbidden sets.

6.2 Topology across the critical levels

For each selected configuration, the Hill region is examined at one regular Jacobi level above the largest critical value, between every consecutive pair of critical values, and below the smallest. Table 9 records the resulting component sequence as C_J decreases. Here A and F denote the numbers of allowed and forbidden components, respectively. At high C_J, $A = 5$: the exterior component and the four primary neighbourhoods are separate. At sufficiently low C_J, $A = 1$ and $F = 0$; apart from the singular primary points, the whole configuration plane is allowed. We refer to this as the whole-plane regime.

Table 9: Connected-component sequences between successive critical Jacobi levels. Each list runs from above the largest to below the smallest critical level.

Configuration	Allowed components A	Forbidden components F
Case 1	(5,4,3,2,2,1,1,1,1,1,1,1)	(1,1,1,1,2,2,3,4,3,2,1,0)
Case 2	(5,4,3,2,1,1,1,1,1,1)	(1,1,1,1,1,2,3,2,1,0)
Generic branch-24 parent	(5,4,3,2,2,1,1,1,1,1)	(1,1,1,1,2,2,3,2,1,0)
Near-H1 branch-24 parent	(5,4,3,2,2,1,1,1,1,1)	(1,1,1,1,2,2,3,2,1,0)
Saddle×centre parent	(5,4,3,2,1,1,1,1,1,1,1,1)	(1,1,1,1,1,2,3,4,3,2,1,0)

The Case-1 sequence shows the two distinct roles of saddle levels. Crossing branches 8, 3, 13 and 15 at

$$C_{J,e} = 3.46, \quad 3.39, \quad 3.26, \quad 3.22$$

reduces the number of allowed components from five to one. The remaining saddles alter the forbidden-set connectivity without changing A, and the four minima subsequently close the remaining forbidden components. Figure 10 shows the first two neck openings. At branch 8 the m_0 and m_1 neighbourhoods join; at branch 3 the combined region connects to the exterior.

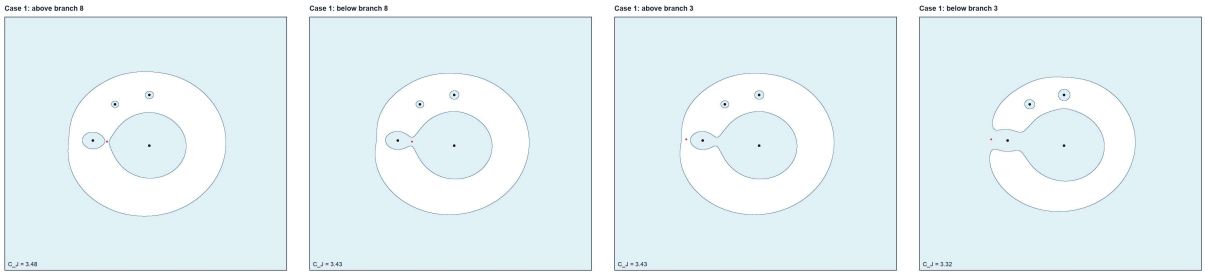


Figure 10: Two successive Case-1 neck openings as C_J decreases. Blue shading is the allowed set, white is forbidden, black circles are the primaries, red points are the critical equilibria, and blue curves are the zero-velocity curves. From left to right, the first pair brackets branch 8 and the second pair brackets branch 3.

The Case-2 reference undergoes an analogous five-to-one merger through branches 22, 20, 23 and 19 at

$$4.84, \quad 4.72, \quad 4.57, \quad 4.51.$$

The generic and near-H1 branch-24 parents have the same component-count sequence, although the critical thresholds and geometric attachments differ. In every selected configuration, the observed global change agrees with the local Morse classification.

The component calculation uses the binary sets $2\Omega \geq C_J$ and $2\Omega < C_J$ with eight-neighbour connectivity. To check the effect of finite computational boundaries, the classification was repeated on

$$[-4,4]^2, \qquad [-6,6]^2, \qquad [-8,8]^2$$

with spatial resolution 0.03. All 54 interval classifications are unchanged under these enlargements. The reported component counts and bounded-hole classifications are therefore insensitive to the chosen box at this resolution.

6.3 Periodic families in the Hill regimes

The Jacobi range of each periodic family can now be placed directly in the critical-level ladder of its parent configuration. The main distinction is already visible for the two modes of a doubly elliptic minimum: the two families leave the same parent equilibrium on opposite sides of its critical Jacobi level.

At the generic branch-24 parent,

$$C_{J,e}^{(24)} = 3.11.$$

G1 remains below this value and therefore lies in the whole-plane regime. G2 remains above it, where the allowed set is connected but one bounded forbidden component remains. Figure 11 shows the largest fixed-amplitude member of each family at its own Jacobi constant.

Table 10: Hill regimes occupied by the five periodic families. $\delta C_J = C_J - C_{J,e}^{\text{parent}}$ is measured from the critical level of the family's own parent equilibrium, so its sign shows which side of that level the family occupies.

Family	$10^3\,\delta C_J$	Hill regime	Threshold crossing
G1	-19.81 to 0.00	whole plane	none
G2	0.00 to 7.12	one forbidden component	none
H1a	-0.52 to 0.00	whole plane	none
H1b	0.00 to 0.43	one forbidden component	none
S1	-39.91 to 0.00	four to two forbidden components	two minima

The same separation occurs at the near-H1 parent, for which

$$C_{J,e}^{(24)} = 3.13.$$

H1a remains below this level and H1b above it throughout both the fixed-amplitude and pseudo-arclength continuations. Even the trusted small-amplitude endpoints closest to the parent lie on opposite sides: the largest H1a value is lower by approximately 8.5×10^{-8}, while the smallest H1b value is higher by approximately 6.9×10^{-8}. The finite-amplitude +1 events occur at $\delta C_J = -5.2 \times 10^{-4}$ for H1a and $\delta C_J = +4.3 \times 10^{-4}$ for H1b. Thus the H1a event lies in the whole-plane regime, whereas the H1b event lies in a regime with one bounded forbidden component.

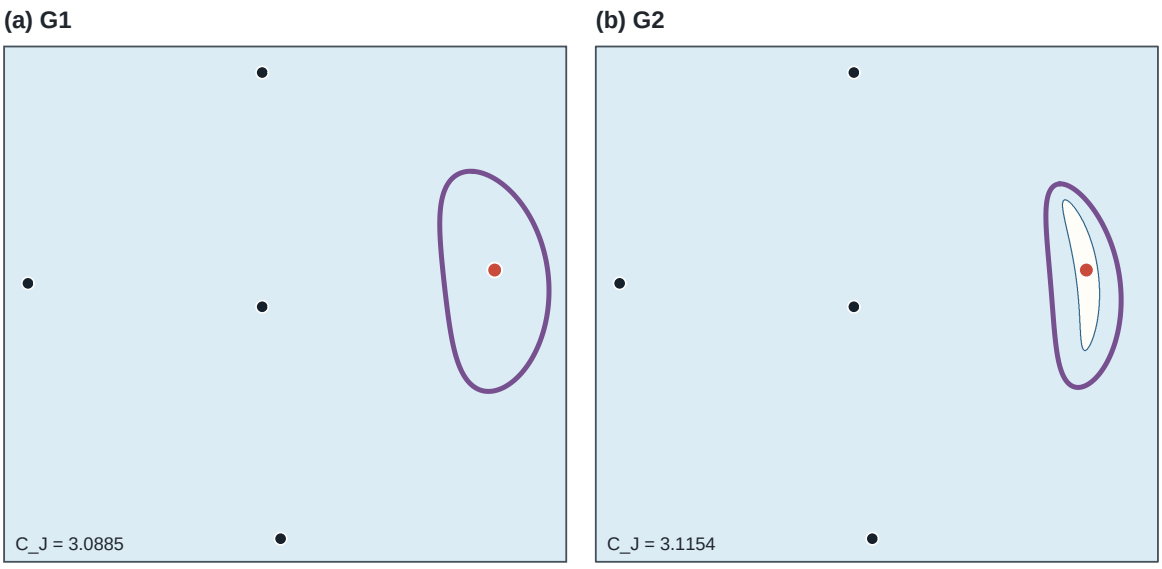


Figure 11: Representative largest fixed-amplitude members of the generic branch-24 families at their respective Jacobi constants. (a) G1 at $C_J = 3.0885$ lies in the whole-plane Hill regime. (b) G2 at $C_J = 3.1154$ surrounds the single bounded forbidden component that persists above the branch-24 minimum. Pale blue denotes the allowed region and white the forbidden region; purple curves are periodic orbits, black circles mark the primaries, and the red point marks their common parent equilibrium.

S1 behaves differently. It begins just below its saddle×centre parent level,

$$C_{J,e}^{(9)} = 3.09,$$

and crosses the two minimum levels

$$C_{J,e}^{(6)} = 3.06, \qquad C_{J,e}^{(1)} = 3.05.$$

The allowed set remains a single component connected to the exterior and to all four primary neighbourhoods, while the forbidden-set count changes $4 \to 3 \to 2$. S1 is therefore the only one of the five computed families whose Jacobi range crosses a Hill-topology threshold.

The Hill geometry therefore complements, but does not replace, the spectral and Floquet classifications. Critical Jacobi levels determine where necks open and bounded forbidden components disappear, while each periodic orbit must remain inside the corresponding allowed set. The distinction between allowed-component connectivity and bounded forbidden components is important: S1 crosses two Hill thresholds without disconnecting the allowed set. Conversely, Hill geometry alone does not determine Floquet stability. G1 and H1a lie in whole-plane regimes, G2 and H1b retain one bounded forbidden component, and S1 crosses two Hill thresholds while remaining Floquet unstable throughout its computed interval.

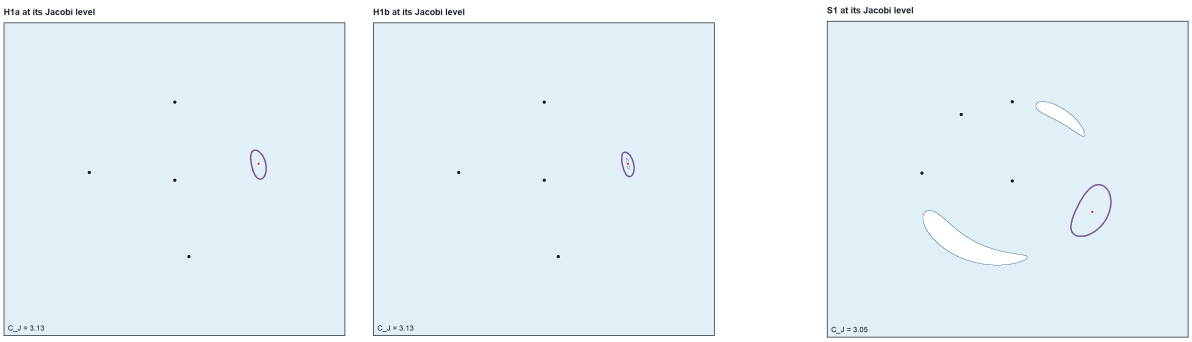


Figure 12: Periodic orbits and their zero-velocity curves. Left: H1a lies in the whole-plane regime, while H1b surrounds one bounded forbidden component. Right: a large S1 member after two forbidden components have closed. All coordinates and primary markers are barycentric.

7 Conclusions

We have formulated and studied a planar restricted five-body problem in which four unequal primaries occupy a general non-symmetric coplanar central configuration. Starting from the central-configuration construction of Shoaib et al. [14], we introduced the barycentric unit-angular-rate normalisation required to place the four primaries at rest in the rotating frame. This allows the equilibrium structure, the linear stability, the periodic-orbit families and the Hill-region geometry of the infinitesimal body to be studied consistently as the primary configuration is varied, without imposing symmetry on the primaries.

In particular, the effective potential gives strong analytical restrictions on the equilibrium set. For nondegenerate configurations the number of equilibria is necessarily odd, and a generic fold creates or annihilates one minimum–saddle pair. Spectral stability is possible only at a minimum and is determined by the trace and determinant conditions obtained from the planar characteristic quartic, in a form analogous to the classical Gascheau–Routh condition. On the investigated slice $(a, b) = (0.90, -0.10)$, two separate positive-mass arcs were found. Along the Case-1 arc the number of equilibria changes from 11 to 13, then to 15, and subsequently back to 13 and 11, while along the Case-2 arc it changes from 9 to 11 and back to 9. These changes occur through six simple folds. The largest equilibrium multiplicity detected on this slice is therefore fifteen; this is not claimed to be a global maximum over the full family of admissible central configurations.

The stability and periodic-orbit calculations reveal a further distinction between the two arcs. Only Case-2 branch 24 contains a doubly elliptic interval. Its two imaginary frequencies approach one another and collide at $s_H = 0.14564$, after which the spectrum leaves the imaginary axis as a complex quartet. From the associated centre modes we continued five representative Lyapunov families: G1 and G2 from a well-separated doubly elliptic equilibrium, H1a and H1b from a parent close to the H1 collision, and S1 from a saddle×centre equilibrium. G1, G2, H1a and H1b retain a unit-circle nontrivial Floquet pair over their initial computed ranges, whereas S1 is Floquet unstable with a real reciprocal pair. The independent continuations of H1a and H1b also identify two distinct transverse finite-amplitude degeneracies at which the nontrivial Floquet pair reaches $+1$. The two events are numerically distinct, although their nonlinear branch type is not determined here.

At the same generic Case-2 branch 24 configuration, three rosette-type circulating periodic families were obtained independently from resonant Kepler seeds. These solutions show that the periodic motion is not confined to local neighbourhoods of equilibria. The generating member of

the exterior P1:2 family has a real reciprocal nontrivial Floquet pair, while the generating members of the interior P2:1 and P3:1 families have their nontrivial pairs on the unit circle.

The Jacobi integral provides the corresponding geometric picture for the local Lyapunov families. The critical Jacobi levels determine where equilibrium necks open and where bounded forbidden components disappear. The families occupy different Hill regimes relative to the critical level of their parent equilibrium: G1 and H1a lie on the whole-plane side of their parent minima, whereas G2 and H1b remain on the side with one bounded forbidden component. S1 is the only one of these five families whose Jacobi range crosses Hill-topology thresholds, passing two minimum levels while remaining Floquet unstable. Equilibrium multiplicity identifies the saddle-node structure, while the equilibrium spectrum locates the stable interval and its Hamiltonian–Hopf boundary. Floquet multipliers classify the computed periodic families. The Hill regions specify the configuration-space domains accessible at their Jacobi constants.

Data and code availability

The source code, machine-readable numerical data, and figure-reproduction scripts supporting this study are available at `https://github.com/drmshoaib/4-1-body-problem`. All state and variational integrations use `DOP853` with rtol = atol = 10^{-12}, and the randomised equilibrium searches use fixed seeds. Unless otherwise stated, displayed values are rounded to two decimal places; additional digits are retained where they are needed to resolve critical-level ordering, identify refined events, or report periodic-orbit data. Jacobi constants of the local Lyapunov families are reported primarily as offsets δC_J from the critical level of their parent equilibrium, whereas the circulating families are reported with their full C_J values. The repository data retain the full working precision used for refinement and validation.

References

[1] Eugene L. Allgower and Kurt Georg. *Introduction to Numerical Continuation Methods*, volume 45 of *Classics in Applied Mathematics*. SIAM, 2003.

[2] A. N. Baltagiannis and K. E. Papadakis. Equilibrium points and their stability in the restricted four-body problem. *International Journal of Bifurcation and Chaos*, 21(8):2179–2193, 2011.

[3] A. N. Baltagiannis and K. E. Papadakis. Families of periodic orbits in the restricted four-body problem. *Astrophysics and Space Science*, 336(2):357–367, 2011.

[4] Brahim Benhammouda, Abdalla Mansur, Muhammad Shoaib, Iharka Szucs-Csillik, and Daniel Offin. Central configurations and action minimizing orbits in kite four-body problem. *Advances in Astronomy*, 2020:5263750, 2020.

[5] Marshall Hampton and Richard Moeckel. Finiteness of relative equilibria of the four-body problem. *Inventiones Mathematicae*, 163(2):289–312, 2006.

[6] Tilemachos J. Kalvouridis. A planar case of the $n + 1$ body problem: the "ring" problem. *Astrophysics and Space Science*, 260(3):309–325, 1999.

[7] Abdul Rehman Kashif and Muhammad Shoaib. Restricted concave kite five-body problem. *Advances in Astronomy*, 2023:9434141, 2023.

[8] Herbert B. Keller. Numerical solution of bifurcation and nonlinear eigenvalue problems. In Paul H. Rabinowitz, editor, *Applications of Bifurcation Theory*, pages 359–384. Academic Press, New York, 1977.

[9] Kenneth R. Meyer, Glen R. Hall, and Dan Offin. *Introduction to Hamiltonian Dynamical Systems and the N-Body Problem*, volume 90 of *Applied Mathematical Sciences*. Springer, 2 edition, 2009.

[10] John Milnor. *Morse Theory*, volume 51 of *Annals of Mathematics Studies*. Princeton University Press, 1963.

[11] Forest Ray Moulton. The straight line solutions of the problem of n bodies. *Annals of Mathematics*, 12(1):1–17, 1910.

[12] A. Ollongren. On a particular restricted five-body problem: an analysis with computer algebra. *Journal of Symbolic Computation*, 6(1):117–126, 1988.

[13] Julian I. Palmore. Measure of degenerate relative equilibria. i. *Annals of Mathematics*, 104(3):421–429, 1976.

[14] Muhammad Shoaib, Brahim Benhammouda, Bonnie A. Steves, and Winston L. Sweatman. Central configurations in the general four body coplanar problem with different masses. Research Square, preprint (Version 1), posted 10 April 2023, 2023. `https://doi.org/10.21203/rs.3.rs-2783132/v1`.

[15] Carles Simó. Relative equilibrium solutions in the four body problem. *Celestial Mechanics*, 18(2):165–184, 1978.

[16] Bonnie A. Steves and Archie E. Roy. Some special restricted four-body problems—I. modelling the Caledonian problem. *Planetary and Space Science*, 46(11–12):1465–1474, 1998.

[17] Victor Szebehely. *Theory of Orbits: The Restricted Problem of Three Bodies*. Academic Press, New York, 1967.

[18] Euaggelos E. Zotos and K. E. Papadakis. Orbit classification and networks of periodic orbits in the planar circular restricted five-body problem. *International Journal of Non-Linear Mechanics*, 111:119–141, 2019.

[19] Euaggelos E. Zotos and Md Sanam Suraj. Basins of attraction of equilibrium points in the planar circular restricted five-body problem. *Astrophysics and Space Science*, 363(1):20, 2018.